

On the Contribution of Phase Separation to Pattern Formation during Normal-Incidence Ion Bombardment of Binary Compounds

Wes Galbraith

September 28, 2017

Abstract

We extend a model of Bradley and Shipman for the normal incidence ion bombardment of binary compounds to account for the effects of competing instabilities caused by the Bradley-Harper effect and ion-induced phase separation. Through a weakly nonlinear analysis and numerical integrations, we find that the phase difference between surface height and composition may serve as a useful indicator of which physical mechanism primarily contributes to the formation of experimentally observed ripples and nanodot arrays. Our numerical simulations also suggest the existence of traveling wave solutions to our equations in the phase separation regime.

1 Introduction

Bombardment of a solid surface by an unfocused ion beam provides a cost-effective alternative to existing lithographic techniques for fabricating a patterned surface. The self-assembled patterns resulting from ion beam sputtering (IBS) are utilized in a number of ways. It has been observed that IBS induced ripple patterns have a wavelength comparable to that of visible light, suggesting their potential use in the manufacture of diffraction gratings [4]. It was suggested in 1976 that IBS patterned surfaces be implemented in the biomedical field to improve the biocompatibility of materials [1]. Since then, rippled surfaces produced by IBS have indeed been used as cell culture substrates that provide mechanical cues which can influence cell adhesion and proliferation, allowing for control over stem cell differentiation [14, 26]. The patterned surfaces formed by IBS have also been used as templates during the fabrication of other materials. Hexagonal nanodot arrays have been used during the creation of hexagonal arrays of nanomagnets, which have potential to be used in high-density magnetic data storage [25]. Ripple patterns serve as a substrate during deposition of a metal. This can lead to the formation of rows of nanoparticles exhibiting a polarization-dependent plasmon absorption, and could be exploited as dichroic filters, or in chemical sensing and catalysis [21]. Finally, preventing pattern formation is of obvious practical interest for the purpose of polishing an optical surface by IBS. Controlling the selected pattern during an IBS process, as well as its geometric properties, will require a thorough understanding of which physical mechanisms make significant contributions to surface dynamics during sputtering. Myriad theories and partial differential equation (PDE) models have been proposed in an attempt to realize this goal.

The foundation on which many PDE models of ion bombardment of amorphous solids rest is the Bradley Harper (BH) theory [4]. Central to the BH theory is the dependence of sputter yield on curvature. Heuristically, the power transferred from sub-surface collision cascades to surface atoms during ion bombardment is enhanced in regions of positive mean curvature (surface minima) due to the proximity of these atoms to cascades initiated at nearby points on the surface. Likewise, less power is deposited in regions of negative mean curvature (surface maxima). This phenomenon has a destabilizing effect on the surface, since it increases the likelihood that atoms in troughs are sputtered due to exceeding the surface bonding energy, while simultaneously decreasing the likelihood that atoms at crests are sputtered. The presence of this instability helps to explain why surfaces undergoing IBS evolve to form ripple patterns, rather than a flat steady state. Using the Sigmund approximation for the distribution of power deposited by collision cascades [24], Bradley and Harper derive analytic expressions for the curvature dependence of sputter yield, and hence the normal component of the surface velocity. Their model, which also incorporates the stabilizing effects of thermally activated surface diffusion, predicts the formation of ripple patterns whose wavevector is parallel to the surface component of the beam direction for near normal angles of incidence and perpendicular for near grazing angles of incidence, and is in agreement with the results of IBS experiments on amorphous surfaces [17].

While the BH model describes ripple formation for an elemental solid, considering the bombardment of a multi-component surface opens a new avenue to pattern formation: the coupling of surface topography to composition. This was demonstrated experimentally by Facsko et. al., who observed the formation of Sb quantum dot arrays on an initially rough surface of GaSb subjected to normal incidence ion bombardment (NIIB) by Ar^+ [9]. This result came somewhat as a surprise, since the physical system associated with NIIB

is isotropic, suggesting that no linearly unstable wavevector should be selected over another. Nevertheless, the dots displayed hexagonal order extending over more than six periods and were normally distributed in diameter with small variance. Other reports of hexagonal patterns formed during NIIB of a multi-phase system were provided for Ge irradiated by heavy Bi^+ and Bi^{++} ions [2, 3], or with Ga^+ ions [10, 29].

Pioneering work towards constructing a coupled PDE model for NIIB of binary solids was conducted by Shenoy, Chan, and Chason (SCC) [22]. While they demonstrated that composition could indeed be coupled to surface topography, and could be controlled to either be in phase or out of phase with surface height, SCC's model was restricted to the linear regime, a limitation preventing the observation of patterns such as hexagonal arrays of nanodots. Bradley and Shipman (BS) later extended the SCC model to account for the effects of momentum transfer from impinging ions to surface atoms [23]. This produced a narrow band of unstable wavenumbers in the linear regime, a prerequisite for the formation of finite-wavelength patterns, as described in the modern theory of pattern formation [7, 12]. The BS model also includes nonlinearities, which were studied using both analytic methods and numerical integrations. Solutions to the BS model suggest that NIIB can lead to the formation of both hexagon and stripe patterns on a binary surface, as well as experimentally observed coarsening of nanodots.

In the BS model, it is assumed that the BH effect destabilizes the surface, similar to its role in the original BH model. After extending the crater function formalism to binary materials [19] and obtaining parameter estimates from molecular dynamics simulations [20], Norris et. al. argued that the BH effect in fact plays a limited role in pattern formation during NIIB of GaSb, and proposed ion induced phase separation as an alternative mechanism [18]. Citing the line compound in the phase diagram of GaSb, Norris hypothesizes that GaSb has a triple-well Gibb's free energy function, with one well corresponding to the homogeneous state, and a well corresponding to each of the two nearly pure states. The rapid sputtering of one component thus leaves the surface in an energetically unfavorable state, and the resulting flow of surface atoms works to locally minimize the free energy, leading to phase separation, and then pattern formation. This work has since come under intense scrutiny. For instance, it has been pointed out that Norris's crater function formalism neglected the effects of curvature dependence, which has been shown to introduce error in parameter estimation [11]. While Norris's generalization of the BS model to include the effects of phase separation did produce a narrow band of unstable wave numbers in the absence of the BH effect, his model does not include the nonlinear effects previously taken into consideration by Bradley and Shipman, and there thus remains more to be said about the role of phase separation in the formation of patterns on a binary surface.

The goal of this work is to investigate the relative influences of phase separation and the BH effect in the nonlinear regime. We begin by deriving a system of coupled PDE's to track the time evolution of small perturbations in surface height and composition from a steady state in section 2. We then perform a linear stability analysis on our model in section 3, in which we demonstrate the presence of narrow bands of linearly unstable wavenumbers for distinct parameter regimes corresponding to both the BH effect and phase separation. As an interesting side result, we observe that our model produces multiple simultaneous narrow bands for specific choices of parameters. In section 4, we derive amplitude equations which describe the evolution of our model in the weakly nonlinear regime. We then describe the spectral method we employed in the numerical integration of our fully nonlinear equations of motion in section 5. We furnish our Python implementation of the numerical method in appendix A. Finally in section 6, we present the results of our numerical integrations. Both our weakly nonlinear analysis and our simulations suggest that stripe and hexagonal patterns are formed in the BH and phase separation parameter regimes. We find two crucial points of distinction between solutions in these two regimes: the phase difference of the surface height and composition in time, and the degree of order in the observed patterns. We also find that a slight perturbation to the relative phase, perhaps caused by the presence of simultaneous linear instabilities, can give rise to traveling wave solutions. We discuss the physical implications of these findings in section 7.

2 Description of the Model

The derivation of our model is a synthesis of the work of Bradley and Shipman [23], and that of Norris [18]. We begin by deriving the linear model, deferring the consideration of nonlinearities until section 4. Suppose that a binary solid composed of elements A and B and with a nominally flat surface is irradiated by a broad ion beam at normal incidence. Further assume that the sputter yield of species B is greater than that of species A . Choose orthonormal coordinates (x, y, z) so that the plane $z = h_0$ gives the average initial surface height for some choice of the constant h_0 , and so that $(0, 0, 1)$ opposes the beam direction. Assume that as the solid is eroded, no overhangs develop, so that at each time t , the surface of the solid may be described by the equation $z = h(x, y, t)$, where $h(x, y, t)$ is a function describing the height of the point on the surface with spatial coordinates (x, y, z) at time t . Let the surface concentration of A atoms at the point $(x, y, h(x, y, t))$ and time t be denoted by $c_s = c_s(x, y, t)$. We expect that as the surface is eroded, an amorphous surface layer of depth Δ (typically a few atoms) will form in which the average value of c_s is greater than the bulk concentration

c_b of A atoms deeper within the solid. We assume that, if the solid is exposed to the ion beam for a sufficiently long time period, then a steady state will develop in which the surface height h recedes at a constant rate v_0 , and the surface concentration of c_s of A atoms tends to a constant $c_{s,0}$. The steady state is thus described by $h = h_0 - v_0 t$ and $c_s = c_{s,0}$. We introduce a perturbation (u, ϕ) to the steady state, so that $h = h_0 - v_0 t + u$ and $c_s = c_{s,0} + \phi$.

In accordance with the BS theory, [23], we assume that the sputter yield F_i of each species is proportional to the power P deposited at the surface of the solid by collision cascades, so that $F_i = \Lambda_i P$ for $i = A, B$ and proportionality constants $\Lambda_i = \Lambda_i(c_s)$. We assume that the power is enhanced at surface minima, so that P takes the functional form $P = P_0 + \alpha \nabla^2 u$, where P_0 is the power deposited on a surface of zero curvature and α is a positive constant.

Changes in the surface height and composition are due to both the flux of sputtered ions from the amorphized surface layer and the flow of atoms within this layer due to surface currents \mathbf{J}_i , for $i = A, B$. From mass conservation, the change in surface height above (x, y) is given by

$$\frac{\partial h}{\partial t} = -\Omega(F_A + F_B + \nabla \cdot \mathbf{J}_A + \nabla \cdot \mathbf{J}_B), \quad (1)$$

where Ω is the atomic volume, which we assume to be the same for both species. The change in surface concentration is as in [23]:

$$\begin{aligned} \Delta \frac{\partial c_s}{\partial t} &= -\Omega(F_A + \nabla \cdot \mathbf{J}_A) - c_b \frac{\partial h}{\partial t} \\ &= \Omega[(c_b - 1)(F_A + \nabla \cdot \mathbf{J}_A) + c_b(F_B + \nabla \cdot \mathbf{J}_B)] \end{aligned} \quad (2)$$

The term $c_b \frac{\partial h}{\partial t}$ in (2) accounts for the replacement of sputtered A atoms in the surface layer with A atoms from the bulk solid.

We are thus left with the task of expressing the equations of motion (1) and (2) in terms of h and c_s . To this end, we assume the surface currents take the form

$$\mathbf{J}_i = -D_{i,e} n_s \nabla \mu_i(c_s) - D_{i,b} n_s \nabla c_i + \frac{D_{i,a} c_i n_s \Omega \gamma_s}{k_B T} \nabla \nabla^2 h - \varrho_i \nabla h, \quad (3)$$

where $c_A := c_s$, $c_B := 1 - c_s$, and $D_{i,e}$, $D_{i,b}$, and $D_{i,a}$ are energetic, ballistic, and Arrhenius diffusivities, respectively. Here n_s is the average number of mobile surface atoms per unit surface area, γ_s is the surface tension, k_B is Boltzmann's constant, T is temperature, μ_A and μ_B are chemical potentials, and ϱ_A and ϱ_B are positive constants.

The first term on the right hand side of (3) captures the effects of energetic chemical diffusion. Following [18], we assume that the surface atoms diffuse so that the concentrations minimize the Ginzburg-Landau free energy functionals

$$E_i(c) := \int_{\mathbb{R}^2} \left(G_i(c) + \frac{\kappa_i}{2} |\nabla c|^2 \right) dx dy,$$

[8], [18]. The functions $G_i = G_i(c)$ are Gibbs's free energy densities for a homogeneous two state system and the κ_i are phase boundary energies which penalize sharp concentration gradients. Chemical potentials $\mu_i = \mu_i(c) := G'_i(c) - \kappa_i \nabla^2 c$ arise as variational derivatives of the E_i . In the specific case we are considering, one may take $G_A(c) = G(c)$ and $G_B(c) = G(1 - c)$ for a single free energy density G , and $\kappa_A = \kappa_B$, but we will continue the derivation in full generality.

The second term in (3) is also from reference [18], and represents the atomic flow resulting from ballistic chemical diffusion. The ballistic diffusion coefficients take the form

$$D_{i,b} = f N_d \pi \int_0^\infty r^3 \rho(r) dr,$$

where f is the flux of the ion beam, N_d is the average number of dislocated atoms per ion impact, and $\rho(r)$ gives the probability that an atom displaced by an ion travels a projected distance of r along the surface.

The third term in (3) models the contribution of surface capillarity to atomic flow [16]. We assume that the potential energy from bonds between neighboring surface atoms in a patch of surface over a region Ω in \mathbb{R}^2 is directly proportional to the surface area of the patch. The potential energy functional for the surface thus takes the form

$$\mathcal{E}(h) = C_0 \int_{\Omega} \sqrt{1 + |\nabla h|^2} dx dy,$$

where C_0 is a positive constant. The variational derivative of the energy functional is therefore

$$\begin{aligned} \frac{\delta \mathcal{E}}{\delta h} &= -C_0 \nabla \cdot \left(\frac{\nabla h}{\sqrt{1 + |\nabla h|^2}} \right) \\ &= -2C_0 H, \end{aligned}$$

where H is the mean curvature of the surface. If we make the standard assumption that $0 < |\nabla h| \ll 1$, then

the small slope approximation for the mean curvature is

$$2H = \frac{\nabla^2 h + |\nabla h|^2(\nabla^2 h - 1)}{(1 + |\nabla h|^2)^{3/2}} \approx \nabla^2 h.$$

The contribution to the flow of surface atoms is then given by

$$-\nabla \frac{\delta \mathcal{E}}{\delta h} = 2C_0 \nabla H \approx 2C_0 \nabla \nabla^2 h.$$

We take $C_0 = \frac{1}{2} \frac{D_{i,a} c_i n_s \Omega \gamma_s}{k_B T}$, so that this term is the third term in equation (3) and agrees with references [18, 23].

The fourth term in equation (3), introduced in [23], accounts for the transfer of momentum from impinging ions to surface atoms, which has the effect of causing atoms to move within the amorphous surface layer against the surface height gradient. The parameters ϱ_i are taken to be positive, and measure the strength of momentum transfer to species i .

At the steady state $h = h_0 - v_0 t$, $c_s = c_{s,0}$, the surface currents \mathbf{J}_A and \mathbf{J}_B vanish, and the sputtered fluxes become $F_i = \Lambda_{i,0} P_0$, where $\Lambda_{i,0} := \Lambda_i(c_{s,0})$. Equations (1) and (2) then give the steady state relations

$$v_0 = \Omega (\Lambda_{A,0} P_0 + \Lambda_{B,0} P_0) \quad (4)$$

and

$$(c_b - 1)\Lambda_{A,0} + c_b \Lambda_{B,0} = 0. \quad (5)$$

We assume that these relations hold for the perturbed steady state $h = h_0 - v_0 t + u$, $c_s = c_{s,0} + \phi$. After substituting the sputtered fluxes F_i and the surface currents \mathbf{J}_i into equations (1) and (2), collecting terms to first order in u and ϕ and their derivatives, and utilizing (4) and (5), we arrive at linear equations of motion for u and ϕ :

$$\begin{aligned} u_t &= A\phi + B\nabla^2 \phi + C\nabla^2 u + D\nabla^2 \nabla^2 u + E\nabla^2 \nabla^2 \phi \\ \phi_t &= A'\phi + B'\nabla^2 \phi + C'\nabla^2 u + D'\nabla^2 \nabla^2 u + E'\nabla^2 \nabla^2 \phi. \end{aligned} \quad (6)$$

The coefficients in (6) are given by

$$\begin{aligned} A &= -\Omega P_0 (\Lambda'_{A,0} + \Lambda'_{B,0}), \\ B &= \Omega n_s (D_{A,e} G''_{A,0} - D_{B,e} G''_{B,0} + D_{A,b} - D_{B,b}), \\ C &= -\Omega (\alpha(\Lambda_{A,0} + \Lambda_{B,0}) - \varrho_A - \varrho_B), \\ D &= -\frac{\Omega^2 n_s \gamma_s}{k_B T} (D_{A,a} c_{s,0} + D_{B,a} (1 - c_{s,0})), \\ E &= -\Omega n_s (\kappa_A D_{A,e} - \kappa_B D_{B,e}), \\ A' &= -\frac{\Omega P_0}{\Delta} ((1 - c_b)\Lambda'_{A,0} - c_b \Lambda'_{B,0}), \\ B' &= \frac{\Omega n_s}{\Delta} ((1 - c_b)(G''_{A,0} D_{A,e} + D_{A,b}) + c_b(G''_{B,0} D_{B,e} + D_{B,b})), \\ C' &= \frac{\Omega}{\Delta} (\varrho_A (1 - c_b) - \varrho_B c_b), \\ D' &= -\frac{\Omega^2 n_s \gamma_s}{\Delta k_B T} ((1 - c_b)D_{A,a} c_{A,0} - c_b D_{B,a} c_{B,0}), \\ E' &= -\frac{\Omega n_s}{\Delta} ((1 - c_b)\kappa_A D_{A,e} + c_b \kappa_B D_{B,e}), \end{aligned}$$

where $\Lambda'_{i,0} := \Lambda'(c_{i,0})$, and $G'_{i,0} := G'(c_{i,0})$. For consistency with [23] and [18], we neglect the B , E , and D' terms, resulting in the simpler model

$$\begin{aligned} u_t &= A\phi + C\nabla^2 u + D\nabla^2 \nabla^2 u \\ \phi_t &= A'\phi + B'\nabla^2 \phi + C'\nabla^2 u + E'\nabla^2 \nabla^2 \phi. \end{aligned} \quad (7)$$

Since species B is preferentially sputtered, we expect the relative surface height to increase at points where concentrations of species A are large, thus we assume that $A > 0$. If the concentration of species A is large in a region of the surface, then the expected number of sputtered A atoms will increase, relative to regions where the concentration of A is small. We therefore assume that $A' < 0$. Finally, the surface must be stable to perturbations with large wavenumbers, which requires that the parameters D and E' are negative. In fact, by analyzing the above expressions for D and E' , we see that $D, E' < 0$.

We seek to further reduce the number of parameters in system (7) by nondimensionalization. To this end, we assume that $u = u_d U$, $(x, y) = x_d(X, Y)$, and $t = t_d T$, where U, X, Y , and T are dimensionless variables, and

u_d , x_d , and t_d are dimension-carrying constants. Equation (7) may be expressed in terms of the dimensionless variables as

$$\begin{aligned} \frac{u_d}{t_d A} \frac{\partial U}{\partial T} &= \phi + \frac{u_d C}{x_d^2 A} \nabla_{X,Y}^2 U + \frac{u_d D}{x_d^4 A} \nabla_{X,Y}^2 \nabla_{X,Y}^2 U \\ -\frac{1}{t_d A'} \frac{\partial \phi}{\partial T} &= -\phi - \frac{B'}{x_d^2 A'} \nabla_{X,Y}^2 \phi - \frac{u_d C'}{x_d^2 A'} \nabla_{X,Y}^2 U - \frac{E'}{x_d^4 A'} \nabla_{X,Y}^2 \nabla_{X,Y}^2 \phi. \end{aligned} \quad (8)$$

We have three dimensional constants to determine. We choose them so that the coefficients of the time derivatives and the fourth order spatial derivative in the first equation scale to have unit magnitude and signs which agree with the coefficients of equation (7). Explicitly, we set $\frac{u_d}{t_d A} = 1$, $\frac{1}{t_d A'} = -1$, and $\frac{u_d D}{x_d^4 A} = -1$. This in turn implies that $t_d = 1/|A'|$, $u_d = A/|A'|$, and $x_d = (|D|/|A'|)^{1/4}$. The nondimensionalized linear system we thus consider is

$$\begin{aligned} u_t &= \phi - a \nabla^2 u - \nabla^2 \nabla^2 u \\ \phi_t &= -\phi + b \nabla^2 u - c \nabla^2 \phi - d \nabla^2 \nabla^2 \phi, \end{aligned} \quad (9)$$

where

$$\begin{aligned} a &= \frac{-C}{|A'|^{1/2} |D|^{1/2}} & b &= \frac{B'}{|A'|^{1/2} |D|^{1/2}} \\ c &= \frac{-AC'}{|A'|^{3/2} |D|^{1/2}} & d &= \frac{|E'|}{|D|}. \end{aligned}$$

Note that the parameter d is positive, which ensures stability of large wavenumber solutions to system (9). We focus on parameters for which there are competing linear instabilities, and thus make the assumption that a is positive.

3 Linear Stability Analysis

To classify parameter regimes of linear instability, we substitute the ansatz

$$\begin{pmatrix} u \\ \phi \end{pmatrix} = \begin{pmatrix} u_* \\ \phi_* \end{pmatrix} \exp(\sigma t + i \mathbf{k} \cdot \mathbf{x})$$

into equation (9) with the goal of deriving a linear dispersion relation expressing $\text{Re}(\sigma)$ as a function of \mathbf{k} . Here u_* and ϕ_* are real constants, $\mathbf{x} = (x, y)^T$, and $\mathbf{k} = (k_x, k_y)^T$. We will denote the magnitude of \mathbf{k} by k . Upon making the aforementioned substitution, we find that σ , $(u_*, \phi_*)^T$ is an eigenvalue, eigenvector pair for the matrix

$$\hat{L} := \begin{pmatrix} ak^2 - k^4 & 1 \\ -bk^2 & -1 + ck^2 - dk^4 \end{pmatrix}.$$

The trace and determinant of \hat{L} are

$$\text{tr}(\hat{L}) = -1 + (a + c)k^2 - (1 + d)k^4,$$

and

$$\det(\hat{L}) = k^2[(-a + k^2)(1 - ck^2 + dk^4) + b]$$

The roots of the characteristic polynomial $p_{\hat{L}}(\sigma) = \sigma^2 - \text{tr}(\hat{L})\sigma + \det(\hat{L})$ are thus

$$\sigma_{\pm} = \frac{\text{tr}(\hat{L}) \pm \sqrt{\text{tr}(\hat{L})^2 - 4 \det(\hat{L})}}{2}.$$

A linear instability is present precisely when the real part of $\sigma_+ = \sigma_+(k)$ is positive for some critical wavenumber k . This, in turn, happens if and only if $\text{tr}(\hat{L}) > 0$ or $\det(\hat{L}) < 0$ for some k . We analyze the cases $0 \leq k \ll 1$ and $k > 0$ separately.

First suppose that $0 \leq k \ll 1$. Since $\sigma_+(0) = 0$, instabilities with wavenumbers on this scale are of type-II, according to the classification in chapter 2 of [7]. To leading order in k ,

$$\text{tr}(\hat{L}) = -1 + \mathcal{O}(k^2),$$

and

$$\det(\hat{L}) = (b - a)k^2 + \mathcal{O}(k^4),$$

so the linearized system exhibits a type-II instability if and only if $a > b$. If this is so, then the imaginary part of σ_+ is zero for small k , hence the instability is of type II-s. For the remainder of the analysis, we will restrict our attention to the case where $a \leq b$. Note that this implies that $b > 0$.

Now assume that $k > 0$. To characterize parameter values at which a linear instability occurs, we consider

the neutral stability surfaces S_{tr} and S_{det} defined by the equations $\text{tr}(\hat{L}) = 0$ and $\det(\hat{L}) = 0$, respectively. Since we have assumed that $k > 0$, the equation for S_{det} can be expressed as $(-a + k^2)(1 - ck^2 + dk^4) + b = 0$. This allows us to define $b = b(k; a, c, d) := (-a + k^2)(-1 + ck^2 - dk^4)$ along S_{det} . To determine the critical value of b , below which there is an instability, we maximize b with respect to k . This yields the critical parameter value $b = b_T := a - (ac + 1)k_T^2 + (ad + c)k_T^4 - dk_T^6$, where k_T is the critical wavenumber

$$k_T := \left(\frac{c + ad + \sqrt{(ad + c)^2 - 3d(ac + 1)}}{3d} \right)^{1/2}.$$

Since k_T is well separated from 0 and the imaginary part of σ_+ is zero for $(k, b) = (k_T, b_T)$, it follows that a type I-s instability is present for choices of parameters that ensure k_T is real and $b < b_T$. In order to observe a narrow band of unstable wavenumbers, we take $b = b_T - \epsilon$, where ϵ is typically 0.05 or 0.1.

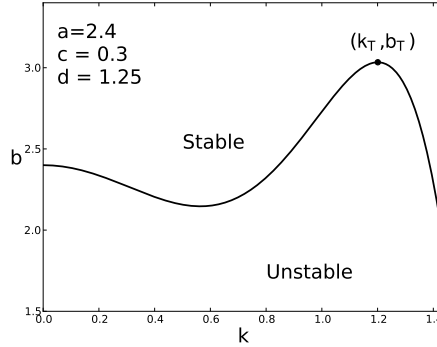


Figure 1: A typical neutral stability curve for S_{det} , assuming that $b_T > a$. Linear instabilities occur for a narrow band of wavenumbers about $k = k_T$ for b just below b_T .

We now consider the other neutral stability surface. Along S_{tr} , we may define $c = c(k; a, d) = k^{-2} - a + (1 + d)k^2$. We minimize c with respect to k to find the critical value of the parameter c , above which an instability is present. By elementary calculus, the minimum value occurs at $c = c_H := -a + 2\sqrt{1 + d}$ at wavenumber $k = k_H := (1 + d)^{-1/4}$. There is thus an instability for $c > -a + 2\sqrt{1 + d}$. The instability is of type I-o if $\det(\hat{L})|_{(k,c)=(k_H,c_H)} > 0$, and is of type I-s if $\det(\hat{L})|_{(k,c)=(k_H,c_H)} < 0$.

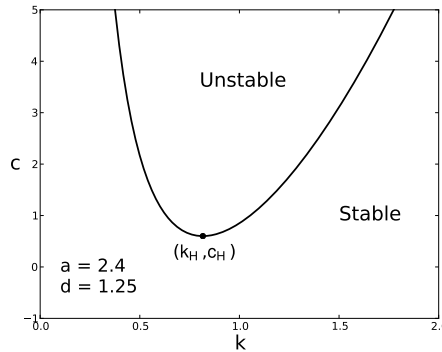


Figure 2: A typical neutral stability curve for S_{tr} . Linear instabilities occur for a narrow band of wavenumbers about $k = k_H$ for $c > c_H$.

We summarize our analysis by describing three regions in (a, c, d) -space in which various behaviors of the linearized system may be expected. We denote by R_3 the set of points (a, c, d) such that there is a type I instability with spatial characteristic wavelength $\frac{2\pi}{k_H}$ for values of c greater than c_H . From our above analysis,

$$R_3 = \left\{ (a, c, d) \in \mathbb{R}^3 : c > -a + 2\sqrt{1 + d} \right\}.$$

We now divide the complement of R_3 in (a, c, d) -space into two regions. By R_1 , we denote the set of points at

which there is a type I-s instability with characteristic wavelength $\frac{2\pi}{k_T}$ for values of b less than b_T . Explicitly,

$$\begin{aligned} R_1 &= \mathbb{R}^3 \setminus R_3 \\ &\cap \{(a, c, d) \in \mathbb{R}^3 : (ad + c)^2 > 3d(ac + 1), c > -da\} \\ &\cap \{(a, c, d) \in \mathbb{R}^3 : (ad + c)^2 > 3d(ac + 1), 1 > -ac\}. \end{aligned}$$

We then define R_2 as the complement of R_1 and R_3 in \mathbb{R}^3 : $R_2 := \mathbb{R}^3 \setminus (R_1 \cup R_3)$. The only instability that may occur in R_2 is a long-wavelength Turing instability, which is present for $b < a$. We emphasize that this instability may also occur outside of R_2 . In figure 3, we plot the three regions in the ac -plane for several fixed values of d . We note that R_1 typically has two connected components, one in which the c coordinate is relatively large compared to the a coordinate, and another where relative magnitudes of the coordinates is reversed. The linear instabilities in these regions are predominantly driven by phase separation and the Bradley-Harper effect, respectively.

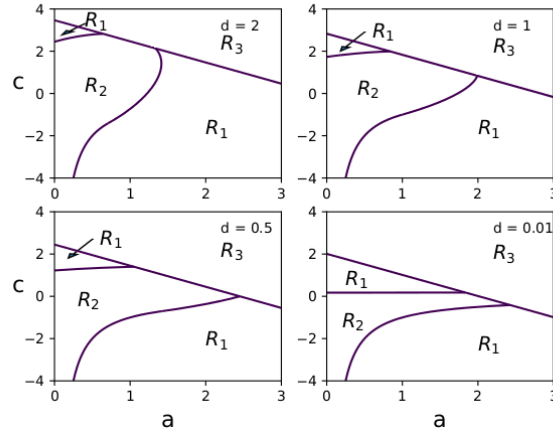


Figure 3: Regions of linear stability plotted in the planes $d = 2, 1, .5, .01$.

It should be noted that our phase diagrams as presented in figure 3 do not capture the regions where a long wavelength instability is present. In fact, such an instability could occur at any point (a, c, d) , provided that $b < a$. It is of interest to know where this instability occurs when b itself depends on a, c , and d , as we may want to isolate an instability, or study the interaction of multiple simultaneous instabilities. Since we will typically set $b = b_T - \epsilon$ for $\epsilon \in \{.05, .1\}$, we include a dashed plot of the curve $a = b_T(a, c, d) - \epsilon$, $\epsilon = 0.1$, in the plot of our linear stability regions shown in figure 4.

We observe a number of linear instabilities in various regions of parameter space. Figure 4 shows specific points in the ac -plane, with $d = 0.5$ fixed, where we plot the linear dispersion relation in figure 5. Panels 1 through 3 of figure 5 show that narrow bands of linearly unstable wavenumbers may arise in diverse regions of parameter space. Panel 1 shows a narrow band that results from the influence of phase separation, while panel 2 shows a narrow band which arises due to the BH-effect. While each of these instabilities are of type I-s, panel 3 shows that type I-o instabilities are present in R_3 near the boundaries with R_1 and R_2 . Panel 4 illustrates a type II-s instability occurring well within the interior of R_2 .

Panels 1-4 of figure 5 essentially replicate the results of [23] and [18], but in panels 5-8, we show that multiple linear instabilities may arise simultaneously near the boundaries of R_1 , R_2 , and R_3 . To the best of our knowledge, this type of result has yet to be presented in the ion bombardment literature. Panel 5 shows simultaneous instabilities of types I-s and I-o, while panel 6 shows type I-s and II-s instabilities, and panel 7 displays type I-o and II-s instabilities. Finally, panel 8 shows that all three types of instabilities may be present simultaneously, provided we choose a point in parameter space near all three regions R_1 , R_2 , and R_3 . The appearance of several competing linear instabilities at the onset of time evolution has potential to create interesting dynamics in the nonlinear regime.

4 Weakly Nonlinear Analysis

In order to observe pattern formation in the phase separation and BH regimes, we must add nonlinearities to the model. Following [23], we add a $|\nabla u|^2$ term to the first equation in system (8) and ϕ^2 and ϕ^3 terms to the second equation. These terms will allow us to reproduce the results of Bradley and Shipman in the BH regime. To study pattern formation in the phase separation regime, we also add a $\nabla^2 \phi^3$ term to the second equation.

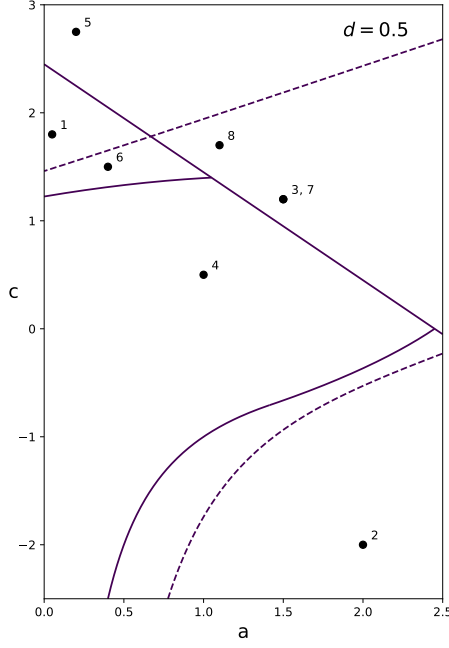


Figure 4: Points in the ac -plane for $d = .5$ used to demonstrate the variety of linear instabilities that arise in the model. Solid lines denote boundaries between regions, while dashed lines show the curve $a = b_T(a, c, d) - \epsilon$, $\epsilon = 0.1$.

This nonlinearity appears in modified Cahn-Hilliard models used to study nanowire formation during thin film growth of binary materials [15]. The nonlinear equations of motion we consider are thus

$$\begin{aligned} u_t &= \phi - a\nabla^2 u - \nabla^2 \nabla^2 u + \lambda |\nabla u|^2 \\ \phi_t &= -\phi + b\nabla^2 u - c\nabla^2 \phi - d\nabla^2 \nabla^2 \phi + \nu \phi^2 + (\eta + \zeta \nabla^2) \phi^3. \end{aligned} \quad (10)$$

We now perform a weakly nonlinear analysis for system (10). We first describe an appropriate function space in which we search for solutions. Let \mathbf{k}_1 , \mathbf{k}_2 , and \mathbf{k}_3 be a triad of unstable wavevectors, with $|\mathbf{k}_j| = k_T$ for $j = 1, 2, 3$ and $\mathbf{k}_i \cdot \mathbf{k}_j = -\frac{\sqrt{3}k_T^2}{2}$ for $i \neq j$. One such triad is illustrated in figure 6. Now define $\mathbf{l}_1 = \frac{8\pi}{k_T^2} \mathbf{k}_1 + \frac{4\pi\sqrt{3}}{k_T^2} \mathbf{k}_2$ and $\mathbf{l}_2 = \frac{4\pi\sqrt{3}}{k_T^2} \mathbf{k}_1 + \frac{8\pi}{k_T^2} \mathbf{k}_2$, and let $\mathcal{L} \subseteq \mathbb{R}^2$ be the lattice generated by \mathbf{l}_1 and \mathbf{l}_2 . Since $\mathbf{k}_i \cdot \mathbf{l}_j = 2\pi\delta_{ij}$ for $i, j = 1, 2$, the dual lattice \mathcal{L}^* is generated by \mathbf{k}_1 and \mathbf{k}_2 . This implies that the functions $e_j(\mathbf{x}) := e^{i\mathbf{k}_j \cdot \mathbf{x}}$ for $j = 1, 2, 3$ are \mathcal{L} -periodic. Since stripe and hexagonal patterns can be realized as linear combinations of these functions, we will consider the subspace of $L^2(\mathbb{R}^2, \mathbb{C})$ consisting of \mathcal{L} -periodic functions V . We define an inner product on V by $\langle f, g \rangle_V := \frac{1}{|\mathcal{P}|} \int_{\mathcal{P}} f(\mathbf{x}) g^*(\mathbf{x}) d\mathbf{x}$, where \mathcal{P} is the parallelogram formed by the convex hull of \mathbf{l}_1 and \mathbf{l}_2 . Observe that e_1, e_2 , and e_3 , along with their complex conjugates, form an orthonormal set with respect to this inner product. We search for solutions $(u, \phi)^T$ to system (10) in the Hilbert space $H = V \oplus V$, with inner product defined by $\langle \mathbf{v}, \mathbf{w} \rangle_H = \langle v_1, w_1 \rangle_V + \langle v_2, w_2 \rangle_V$ for $\mathbf{v} = (v_1, v_2)^T$ and $\mathbf{w} = (w_1, w_2)^T$ in H .

We assume that the point (a, c, d) is in region I and that a long wavelength linear instability is not present, that is, the inequalities $(ad + c)^2 > 3d(ac + 1)$, $b > a$, and $c > -a + 2(1 + d)^{1/2}$ are satisfied. Furthermore, we assume that the control parameter b is just below its critical value $b_T = a - (ac + 1)k_T^2 + (ad + c)k_T^4 - dk_T^6$, where $k_T = \left(\frac{c + ad + \sqrt{(ad + c)^2 - 3d(ac + 1)}}{3d} \right)^{1/2}$ is the critical wavenumber. To this end, we write $b = b_T - \epsilon b_1 + \mathcal{O}(\epsilon^2)$ for $0 < \epsilon \ll 1$. We expand u and ϕ in powers of ϵ about the steady state solution $(u, \phi) = (0, 0)$, so that

$$\begin{aligned} u &= \epsilon u_1 + \epsilon^2 u_2 + \mathcal{O}(\epsilon^3) \\ \phi &= \epsilon \phi_1 + \epsilon^2 \phi_2 + \mathcal{O}(\epsilon^3). \end{aligned}$$

Finally, since the amplitudes evolve on a slow time scale, we distinguish between fast and slow time variables $t_0 = t$ and $t_1 = \epsilon t$, respectively. This implies that $\frac{\partial}{\partial t} = \frac{\partial}{\partial t_0} + \epsilon \frac{\partial}{\partial t_1}$.

After substituting the above expansions into the nonlinear system of PDE's and collecting powers of ϵ , we

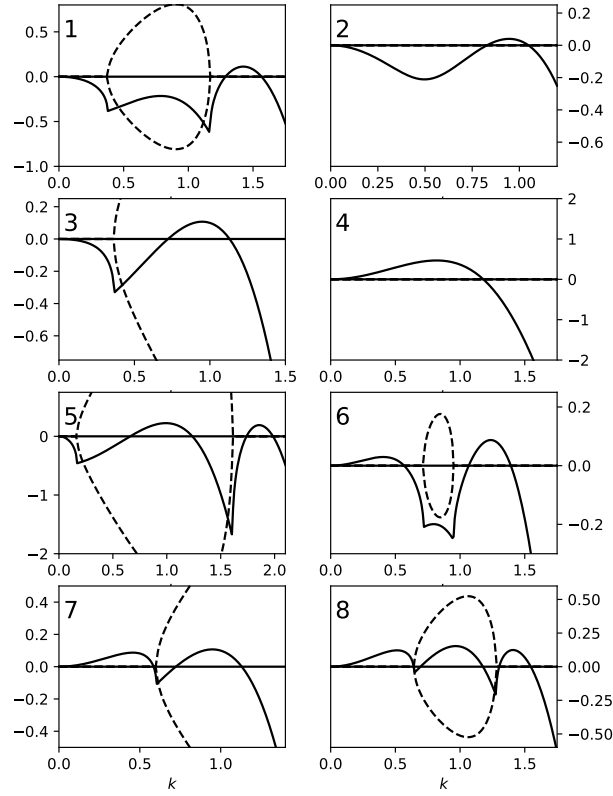


Figure 5: Linear growth rate as a function of wave-number for various points in parameter space. Solid lines represent the real part of σ_+ , while dashed lines show the imaginary parts of σ_{\pm} . Numbers in the top left corner of each plot correspond to labels on points from figure 4.

obtain a system at order ϵ and another system at order ϵ^2 . In increasing order of ϵ , these are

$$L_0 \begin{pmatrix} u_1 \\ \phi_1 \end{pmatrix} = 0, \quad (11)$$

and

$$L_0 \begin{pmatrix} u_2 \\ \phi_2 \end{pmatrix} = \mathbf{q}_2, \quad (12)$$

where

$$L_0 = \begin{pmatrix} \frac{\partial}{\partial t_0} + a\nabla^2 + \nabla^2\nabla^2 & -1 \\ -b_T\nabla^2 & \frac{\partial}{\partial t_0} + 1 + c\nabla^2 + d\nabla^2\nabla^2 \end{pmatrix},$$

and

$$\mathbf{q}_2 = \begin{pmatrix} -\frac{\partial u_1}{\partial t_1} + \lambda(\nabla u_1)^2 \\ -\frac{\partial \phi_1}{\partial t_1} - b_1\nabla^2 u_1 + \nu\phi_1^2 + (\hat{\eta} + \hat{\zeta}\nabla^2)\phi_1^3 \end{pmatrix}. \quad (13)$$

Here we have introduced scaled parameters $\hat{\eta} = \epsilon\eta$ and $\hat{\zeta} = \epsilon\zeta$ of order 1. Since we are interested in finding hexagonal patterns, we seek solutions to the order ϵ system of the form

$$\begin{pmatrix} u_1 \\ \phi_1 \end{pmatrix} = \begin{pmatrix} G \\ 0 \end{pmatrix} + \begin{pmatrix} u_* \\ \phi_* \end{pmatrix} \sum_{j=1}^3 (A_j e^{i\mathbf{k}_j \cdot \mathbf{x}} + A_j^* e^{-i\mathbf{k}_j \cdot \mathbf{x}}),$$

where $u_*, \phi_* \in \mathbb{R}$ are to be determined, $|\mathbf{k}_j| = k_T$ for $j = 1, 2, 3$, and $\mathbf{k}_1 + \mathbf{k}_2 + \mathbf{k}_3 = \mathbf{0}$, so that the \mathbf{k}_j form a triad of unstable wavevectors. The Goldstone mode G and the amplitudes A_1, A_2 , and A_3 are complex valued functions of the slow time parameter t_1 . Observe that u_1 and ϕ_1 as given above are invariant under the transformations $\mathbf{x} \mapsto \mathbf{x} + \mathbf{l}_i$ for $i = 1, 2$, so $(u_1, \phi_1)^T \in H$.

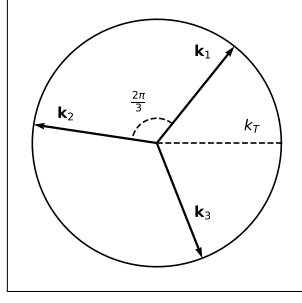


Figure 6: Circle of linearly unstable modes, along with a selected triad of unstable modes that resonate to produce hexagonal patterns in the nonlinear regime.

Since L_0 is linear, to solve the order ϵ problem, it suffices to find elements of $\ker L_0$ of the form

$$\begin{pmatrix} u_1 \\ \phi_1 \end{pmatrix} = \begin{pmatrix} u_* \\ \phi_* \end{pmatrix} e^{i\mathbf{k} \cdot \mathbf{x}}$$

with $|\mathbf{k}| = k_T$. Substituting into the order ϵ equation, this implies that $(u_*, \phi_*)^T$ is an element of $\ker \widehat{L}_0$, where

$$\widehat{L}_0 = \begin{pmatrix} -ak_T^2 + k_T^4 & -1 \\ b_T k_T^2 & 1 - ck_T^2 + dk_T^4 \end{pmatrix}.$$

Since

$$\begin{aligned} \det(\widehat{L}_0) &= k_T^2 [(-a + k_T^2)(1 - ck_T^2 + dk_T^4) + b_T] \\ &= k_T^2 [-b_T + b_T] \\ &= 0, \end{aligned}$$

the nullity of \widehat{L}_0 is 1. It is readily checked that the vector $(1, -ak_T^2 + k_T^4)^T$ is an element of $\ker \widehat{L}_0$. Any element of H of the form

$$\begin{pmatrix} u_1 \\ \phi_1 \end{pmatrix} = \begin{pmatrix} G \\ 0 \end{pmatrix} + \begin{pmatrix} 1 \\ -ak_T^2 + k_T^4 \end{pmatrix} \sum_{j=1}^3 (A_j e^{i\mathbf{k}_j \cdot \mathbf{x}} + A_j^* e^{-i\mathbf{k}_j \cdot \mathbf{x}}) \quad (14)$$

is thus a solution to the order ϵ problem. We are now left to derive amplitude equations which describe the evolution of the A_j 's with the slow time parameter t_1 .

The amplitude equations arise as solvability conditions for the order ϵ^2 system. Namely, we find ordinary differential equations satisfied by the amplitudes which ensure that \mathbf{q}_2 is in the image of the linear operator L_0 . By the Fredholm alternative $\text{im } L_0 = (\ker L_0^\dagger)^\perp$, so instead we may seek equations for the A_j which guarantee that \mathbf{q}_2 is orthogonal to the kernel of the adjoint operator L_0^\dagger [12, 28].

By a lengthy computation, which we provide in Appendix B, the adjoint is given by

$$L_0^\dagger = \begin{pmatrix} \frac{\partial}{\partial t_0} + a\nabla^2 + \nabla^2 \nabla^2 & -b_T \nabla^2 \\ -1 & \frac{\partial}{\partial t_0} + 1 + c\nabla^2 + d\nabla^2 \nabla^2 \end{pmatrix}.$$

Now we determine elements of $\ker L_0^\dagger$ of the form

$$\mathbf{v} = \begin{pmatrix} u_{**} \\ v_{**} \end{pmatrix} e^{i\mathbf{k} \cdot \mathbf{x}},$$

where $|\mathbf{k}| = k_T$ and $(u_{**}, v_{**})^T$ is a constant vector which is necessarily contained in the kernel of $\widehat{L}_0^\dagger = \widehat{L}_0^T$. Since $\det(\widehat{L}_0^T) = \det(\widehat{L}_0) = 0$, it follows that the nullity of \widehat{L}_0^\dagger is 1. It is readily checked that $\mathbf{v}_2 := (1 - ck_T^2 + dk_T^4, 1)^T$ is an element of $\ker \widehat{L}_0^\dagger$. Thus for $j = 1, 2, 3$, the functions $\mathbf{v}_2(\mathbf{k}_j) := \mathbf{v}_2 e^{i\mathbf{k}_j \cdot \mathbf{x}}$, along with their conjugates, are elements of $\ker L_0^\dagger$. An additional element of $\ker L_0^\dagger$ is $\mathbf{v}_1 := (1, 1)^T$.

Now we derive the conditions that lead the coefficients $\langle \mathbf{v}_1, \mathbf{q}_2 \rangle_H$, and $\langle \mathbf{v}_2(\mathbf{k}_j), \mathbf{q}_2 \rangle_H$ to vanish. In what follows, let $\mathbf{f}_1 = (1, 0)^T$ and $\mathbf{f}_2 = (0, 1)^T$. Upon substituting the right side of equation (14) for $(u_1, \phi_1)^T$ in equation (13), and collecting coefficients of 1 and $e^{i\mathbf{k}_j \cdot \mathbf{x}}$ in the first and second component of \mathbf{q}_2 , we find

$$\langle \mathbf{q}_2, \mathbf{f}_1 e^{i\mathbf{k}_i \cdot \mathbf{x}} \rangle_H = -\dot{A}_i + \lambda k_T^2 A_j^* A_k^*,$$

and

$$\begin{aligned}\langle \mathbf{q}_2, \mathbf{f}_2 e^{i\mathbf{k}_i \cdot \mathbf{x}} \rangle_H &= -(-ak_T^2 + k_T^4) \dot{A}_1 + b_1 k_T^2 A_i \\ &\quad + 2\nu(-ak_T^2 + k_T^4)^2 A_j^* A_k^* \\ &\quad + 3(\hat{\eta} - k_T^2 \hat{\zeta})(-ak_T^2 + k_T^4)^3 A_i (|A_i|^2 + 2(|A_j|^2 + |A_k|^2)),\end{aligned}$$

where $i, j, k \in \{1, 2, 3\}$ are ordered cyclically. We also compute

$$\langle \mathbf{q}_2, \mathbf{f}_1 \rangle_H = -\dot{G} + 2\lambda k_T^2 \sum_{j=1}^3 |A_j|^2,$$

and

$$\langle \mathbf{q}_2, \mathbf{f}_2 \rangle_H = 2\nu(-ak_T^2 + k_T^4)^2 \sum_{j=1}^3 |A_j|^2 + 12(\hat{\eta} - k_T^2 \hat{\zeta})(-ak_T^2 + k_T^4)^3 \text{Re}(A_1 A_2 A_3).$$

To derive the equation for A_i , we use the solvability condition for $\mathbf{v}_2(\mathbf{k}_i)$:

$$\begin{aligned}0 &= \langle \mathbf{q}_2, \mathbf{v}_2(\mathbf{k}_i) \rangle \\ &= (1 - ck_T^2 + dk_T^4) \langle \mathbf{q}_2, \mathbf{f}_1 e^{i\mathbf{k}_i \cdot \mathbf{x}} \rangle_H + \langle \mathbf{q}_2, \mathbf{f}_2 e^{i\mathbf{k}_i \cdot \mathbf{x}} \rangle_H \\ &= (-1 + (a+c)k_T^2 - (1+d)k_T^4) \dot{A}_i + b_1 k_T^2 A_i + [\lambda k_T^2 (1 - ck_T^2 + dk_T^4) + 2\nu(-ak_T^2 + k_T^4)^2] A_j^* A_k^* \\ &\quad + 3(\hat{\eta} - k_T^2 \hat{\zeta})(-ak_T^2 + k_T^4)^3 A_i (|A_i|^2 + 2(|A_j|^2 + |A_k|^2))\end{aligned}$$

Solving for \dot{A}_i and transforming time derivatives from the slow time variable $t_1 = \epsilon t$ back to t , we arrive at the amplitude equations

$$\dot{A}_i = \sigma A_i + \tau A_j^* A_k^* - \gamma A_i (|A_i|^2 + 2(|A_j|^2 + |A_k|^2)), \quad (15)$$

where

$$\begin{aligned}\sigma &= \frac{(b_T - b)k_T^2}{1 - (a+c)k_T^2 + (1+d)k_T^4}, \\ \tau &= \frac{\lambda k_T^2 (1 - ck_T^2 + dk_T^4) + 2\nu(ak_T^2 - k_T^4)^2}{1 - (a+c)k_T^2 + (1+d)k_T^4},\end{aligned} \quad (16)$$

and

$$\gamma = \frac{3(\eta - k_T^2 \zeta)(ak_T^2 - k_T^4)^3}{1 - (a+c)k_T^2 + (1+d)k_T^4}.$$

Similarly, we obtain an equation for G by using the solvability condition for \mathbf{v}_1 :

$$\begin{aligned}0 &= \langle \mathbf{q}_2, \mathbf{v}_2 \rangle_H \\ &= \langle \mathbf{q}_2, \mathbf{f}_1 \rangle_H + \langle \mathbf{q}_2, \mathbf{f}_2 \rangle_H \\ &= -\dot{G} + 2\lambda k_T^2 \sum_{j=1}^3 |A_j|^2 + 2\nu(-ak_T^2 + k_T^4)^2 \sum_{j=1}^3 |A_j|^2 \\ &\quad + 12(\hat{\eta} - k_T^2 \hat{\zeta})(-ak_T^2 + k_T^4)^3 \text{Re}(A_1 A_2 A_3).\end{aligned}$$

Thus

$$\dot{G} = 2(\lambda k_T^2 + \nu(-ak_T^2 + k_T^4)^2) \sum_{j=1}^3 |A_j|^2 + 12(\eta - k_T^2 \zeta)(-ak_T^2 + k_T^4)^3 \text{Re}(A_1 A_2 A_3). \quad (17)$$

The general form of the amplitude equations has been well studied [12, 23]. The system exhibits three classes of equilibria, each of which corresponds to a pattern that emerges in solutions of the nonlinear PDE. The stability of the equilibria is governed by the order parameter

$$\xi = \frac{\sigma\gamma}{\tau^2}.$$

The first equilibrium $A_1 = A_2 = A_3 = 0$ corresponds to a homogeneous steady state solution of the PDE. The second class of equilibria consists of the six points $(\pm(\sigma/\gamma)^{1/2}, 0, 0)$, $(0, \pm(\sigma/\gamma)^{1/2}, 0)$, and $(0, 0, \pm(\sigma/\gamma)^{1/2})$, each of which corresponds to a stripe pattern with characteristic wavelength $\frac{2\pi}{k_T}$. The final equilibrium is $A_1 = A_2 = A_3 = \frac{\tau(1+\sqrt{1+20\xi})}{10\gamma}$, which corresponds to a hexagonal nanodot pattern if $A_j > 0$ for $j = 1, 2, 3$, or a hexagonal nanohole pattern if $A_j < 0$ for $j = 1, 2, 3$.

The stability of the equilibria depends on the order parameter ξ as follows: for $\xi \leq -\frac{1}{20}$, only the homogeneous steady state is stable; for $-\frac{1}{20} < \xi < 0$, the homogeneous state remains stable, and the equilibrium giving rise to hexagonal patterns gains stability; for $0 \leq \xi < 1$, the homogeneous steady state loses stability, and the hexagonal state remains stable; for $1 \leq \xi < 4$ the stripe steady state gains stability, while the hexagonal

state is still stable; and for $\xi \geq 4$, only the stripe steady state is stable.

As we shall later see, the phase difference of u and ϕ is a crucial point of distinction between solutions to (10) that arise from the BH-effect and phase separation. For solutions of the form (14), the sign of the second component of the eigenvector $(1, -ak_T^2 + k_T^4)^T$ completely determines whether u and ϕ are in-phase or have a phase difference of π radians. This, in turn, is determined by the sign of the quantity $\varpi := c - 2ad + \sqrt{(ad + c)^2 - 3d(ac + 1)}$. In figure 7, we plot $\text{sgn}(\varpi)$ in the ac -plane for several fixed values of d . We observe that $\varpi > 0$ in the component of R_1 corresponding to phase separation, indicating that u and ϕ will be in phase in this parameter regime. In contrast, $\varpi < 0$ in the component of R_1 which corresponds to the BH effect, and thus we expect a phase difference of π radians in u and ϕ for the solutions in this region. We also point out that ϖ depends only on coefficients of linear terms in system (10), indicating that the relative strengths of the BH effect and phase separation are what cause this shift in phase difference.

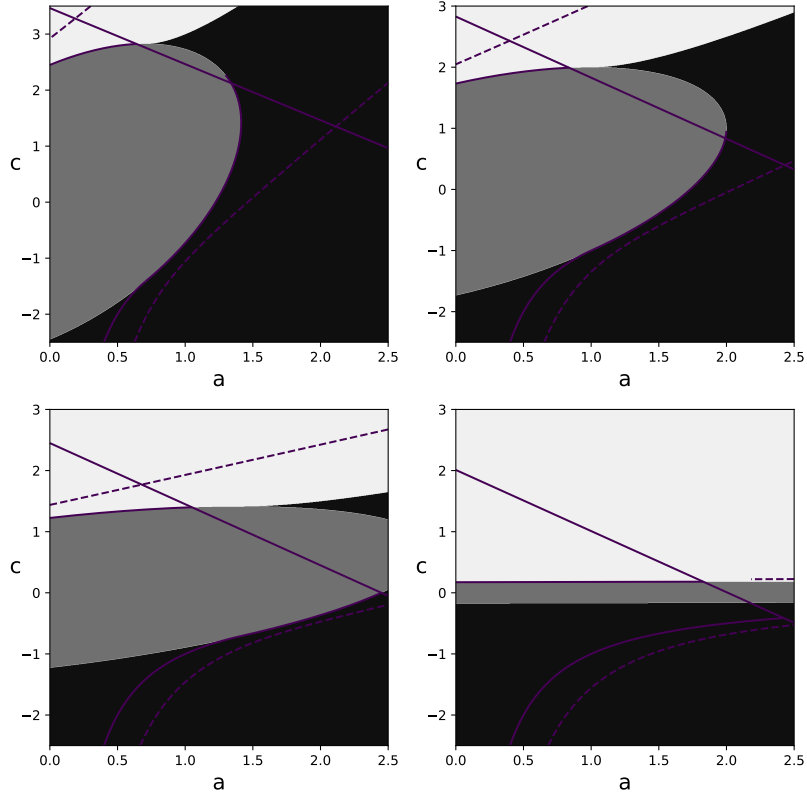


Figure 7: Plots of $\text{sgn}(\varpi)$ in the planes $d = 2$ (top-left), $d = 1$ (top-right), $d = .5$ (bottom-left), and $d = .01$ (bottom-right). Light gray shading indicates that $\text{sgn}(\varpi) = 1$, dark gray shading that $\text{sgn}(\varpi) = -1$, and the intermediate shade of gray within the ellipse $(ad + c)^2 < 3d(ac + 1)$ indicates where ϖ is undefined. The boundaries of regions R_1 , R_2 , and R_3 are overlaid.

5 Numerical Method

We now provide the details of the exponential time differencing method used to approximate the solutions of system (10). The ETDRK4 method that we use was derived by Cox and Matthews [5], was later improved upon by Trefethan and Kassam [13], and is nicely described for reaction diffusion systems by Craster and Sassi [6]. ETDRK4 falls under the broader class of Galerkin methods, which approximate the coefficients in an expansion of the solution to a PDE in an orthogonal basis. For our purposes, we use a cosine expansion, and seek a solution to system (10) with periodic boundary conditions on a square domain of length L . Even though real ion bombardment experiments are not performed with periodic boundary conditions, we argue that the spatial domain is large enough to mitigate the effects of boundary conditions well within the interior of the domain.

We Fourier transform system (10) to obtain an infinite-dimensional system of ODE's:

$$\begin{aligned}\hat{u}_t &= \hat{\phi} + ak^2\hat{u} - k^4\hat{u} + \mathcal{F}[\lambda(\nabla u)^2] \\ \hat{\phi}_t &= -\hat{\phi} - bk^2\hat{u} + ck^2\hat{\phi} - dk^4\hat{\phi} + \mathcal{F}[\nu\phi^2 + \eta\phi^3].\end{aligned}\tag{18}$$

Here $k = |\mathbf{k}|$, and there is one 2-dimensional system of equations for each value of k . We discretize the set of wavevectors at which we solve the system, thereby approximating system (18) with a finite-dimensional system. The wavenumbers we consider form a regularly spaced grid on the rectangle $[0, \frac{\pi N}{2L}] \times [-\frac{\pi N}{2L}, \frac{\pi(N-1)}{2L}]$ in Fourier space. Labeling the wavevectors in the grid $\mathbf{k}_1, \dots, \mathbf{k}_M$, and the corresponding coefficients by $\hat{u}(\mathbf{k}_j), \hat{\phi}(\mathbf{k}_j)$ for $j = 1, \dots, M$, the finite dimensional system of ODE's takes the form

$$\hat{\rho}_t = \mathbf{L}\hat{\rho} + \mathbf{N}(\hat{\rho}),$$

where $\hat{\rho} = (\hat{u}(\mathbf{k}_1), \hat{\phi}(\mathbf{k}_1), \dots, \hat{u}(\mathbf{k}_M), \hat{\phi}(\mathbf{k}_M))^T$, and \mathbf{L} and \mathbf{N} are linear and nonlinear operators, respectively.

Numerous choices exist for arranging the terms in the ODE's into a linear and nonlinear part. We include only diagonal linear terms in \mathbf{L} , so that $\mathbf{L} = \text{diag}(ak_1^2 - k_1^4, ck_1^2 - dk_1^4, \dots, ak_m^2 - k_m^4, ck_m^2 - dk_m^4)$. The primary reason for doing this is to simplify computations of matrix exponentials in our implementation of the method. The nonlinear operator then takes the form $\mathbf{N} = (\iota_u \circ \mathcal{F} \circ R_1 \circ \mathcal{F}^{-1} \circ G_u, \iota_\phi \circ \mathcal{F} \circ R_2 \circ \mathcal{F}^{-1} \circ G_\phi)^T$, where G_u and G_ϕ map $\hat{\rho}$ to the rectangular grids of wavenumbers, ι_u and ι_ϕ include the wavevectors back into their correct entries in the vector $\hat{\rho}$, and $R_1(u, \phi) = \phi + \lambda|\nabla u|^2$ and $R_2(u, \phi) = -\phi + \nu\phi^2 + (\eta + \zeta\nabla^2)\phi^3 + b\nabla^2 u$ are the operators from the “right hand side” of the nonlinear evolution equations. The Laplacian in the linear term $b\nabla^2 u$ in R_2 is approximated with a spectral derivative [27], while the derivatives in the nonlinear terms $\lambda|\nabla u|^2$ and $\zeta\nabla^2\phi^3$ are computed with a second order finite difference method. We note that the choice to use finite differences results in a loss of accuracy, from $\mathcal{O}(h^4)$ to $\mathcal{O}(h^2)$ in the step size h , but it is a cost we are willing to pay in return for ease of implementation.

Once we have cast our numerical problem in this form, we employ the ETDRK4 scheme from [5]. Given a step size h , we advance the approximate solution $\hat{\rho}_n$ from time t_n to $t_{n+1} = t_n + h$ via the scheme

$$\begin{aligned}\mathbf{a}_n &= e^{\mathbf{L}h/2}\hat{\rho}_n + h\kappa(\mathbf{L}h/2)\mathbf{N}(\hat{\rho}_n) \\ \mathbf{b}_n &= e^{\mathbf{L}h/2}\hat{\rho}_n + h\kappa(\mathbf{L}h/2)\mathbf{N}(\mathbf{a}_n) \\ \mathbf{c}_n &= e^{\mathbf{L}h/2}\mathbf{a}_n + h\kappa(\mathbf{L}h/2)(2\mathbf{N}(\mathbf{b}_n) - \mathbf{N}(\hat{\rho}_n)) \\ \hat{\rho}_{n+1} &= e^{\mathbf{L}h}\hat{\rho}_n + h\alpha(\mathbf{L}h)\mathbf{N}(\hat{\rho}_n) \\ &\quad + 2h\beta(\mathbf{L}h)(\mathbf{N}(\mathbf{a}_n) + \mathbf{N}(\mathbf{b}_n)) \\ &\quad + h\gamma(\mathbf{L}h)\mathbf{N}(\mathbf{c}_n).\end{aligned}\tag{19}$$

The coefficients $\kappa(\mathbf{L}h/2)$, $\alpha(\mathbf{L}h)$, $\beta(\mathbf{L}h)$, and $\gamma(\mathbf{L}h)$ are computed by evaluating the complex valued functions

$$\begin{aligned}\kappa(z) &= \frac{e^z - 1}{z} \\ \alpha(z) &= \frac{-4 - z + e^z(4 - 3z + z^2)}{z^3} \\ \beta(z) &= \frac{2 + z + e^z(-2 + z)}{z^3} \\ \gamma(z) &= \frac{-4 - 3z - z^2 + e^z(4 - z)}{z^3}\end{aligned}$$

at the appropriate linear operator. There is a well studied numerical instability caused by cancellation error that arises in evaluating these functions if an eigenvalue of $\mathbf{L}h/2$ or $\mathbf{L}h$ is near the origin. We avoid the instability by adhering to advice given in [13], namely to use Cauchy's integral formula to compute the coefficients in (19). So for $f \in \{\kappa, \alpha, \beta, \gamma\}$, we have, for instance

$$f(\mathbf{L}h) = \frac{1}{2\pi i} \int_{\Gamma} f(z)(zI - \mathbf{L}h)^{-1},$$

where Γ is any contour in the complex plane which encloses the eigenvalues of $\mathbf{L}h$. In practice, we take Γ to be a union of circles of radius r centered at the eigenvalues λ . In our case, the eigenvalues of Lh are real, so we may use symmetry to compute the coefficients via the integral

$$f(\mathbf{L}h) = \frac{r}{\pi} \int_0^\pi f(\lambda + re^{it})((\lambda + re^{it})I - \mathbf{L}h)^{-1} dt.$$

These computations are performed before the main ETDRK4 loop, and require a relatively small overhead cost. We provide our Python implementation of the numerical method in appendix A.

6 Numerical Results

We now exhibit the various properties of solutions to system (10) using the numerical method sketched in the previous section. We will sequentially discuss the regions R_1 , R_2 , and R_3 of linear parameter space.

Recall that the region R_1 typically has two connected components for the values of d that we consider, one corresponding to the instability from the BS model, and the other corresponding to the instability caused by phase separation. We will denote these connected components by C_{BS} and C_{PS} . Within C_{BS} , we replicated the results of Bradley and Shipman [23]. Namely, we found stripe patterns for parameters such that $\xi > 4$ and hexagonal patterns for $0 < \xi < 1$. Hexagons from C_{BS} are shown in figure 8, while stripes from C_{BS} are displayed in figure 9. The degree of order of the patterns varied within C_{BS} from highly ordered stripes and hexagons to stripes with non-constant local wavevectors and hexagons with dislocations. The later defects are similar to those observed in real ion bombardment experiments [9]. In addition, the height and composition fields u and ϕ appear to be anti-correlated for solutions within C_{BS} .

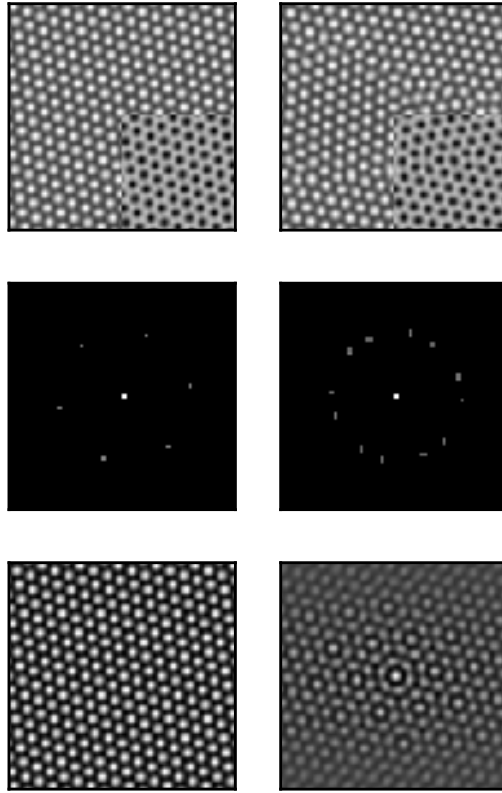


Figure 8: Hexagonal patterns in C_{BS} . The left column shows well ordered hexagons for parameter values $a = 2.25$, $b = b_T - .05 \approx 3.7898$, $c = -2$, $d = .1$, $\lambda = .1$, $\nu = 1$, $\eta = 10$, $\zeta = 0$. The right column shows less well ordered hexagons at parameter values $a = 2.25$, $b = b_T - .05 \approx 3.1862$, $c = -1.5$, $d = .1$, $\lambda = .1$, $\nu = 1$, $\eta = 10$, $\zeta = 0$. The first row shows u at $t = 2000$ with $L = 60$ (ϕ inset). The second row shows the power spectral density function of u . The third row shows the autocorrelation function of u . Light shading denotes positive values, while dark shading demarks negative values.

Solutions resulting from parameters in C_{PS} , like those in C_{BS} , exhibit stripe and hexagonal patterns, as we show in figures 10 and 11. However, whereas the fields u and ϕ were anti-correlated for solutions in C_{BS} , they appear to be positively correlated within C_{PS} , as we illustrate in figure 12. This suggests that phase separation would lead the preferentially sputtered species to predominantly populate surface maxima. In addition, the solutions we observed in the C_{PS} component appear to be remarkably well ordered, more so than the experimental surfaces, and we conjecture that this holds in general for solutions in C_{PS} . Of course,

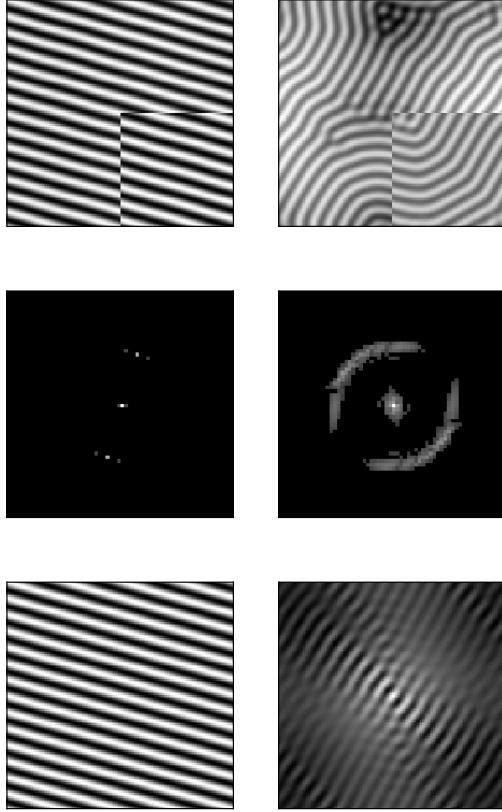


Figure 9: Stripe pattern from C_{BS} . Parameter values for the first column are $a = 2.25$, $b = b_T - .05 \approx 2.5987$, $c = .25$, $d = 1.25$, $\lambda = .25$, $\nu = .1$, $\eta = 20$, $\zeta 0$, $t = 1200$, $L = 40$, and those for the second column are $a = 2.25$, $b = b_T - .05 \approx 2.6110$, $c = -1$, $d = .1$, $\lambda = .1$, $\nu = .1$, $\eta = 10$, $\zeta = 0$, $t = 2000$, $L = 60$. The second and third rows show power spectral density and autocorrelation functions.

unobserved solutions with defects could still exist for parameters in C_{PS} , despite the results of our numerics. Proof of their non-existence, or even precisely stating what we mean by a “well ordered” solution, will require tools from algebraic topology, namely persistent homology. Another avenue to illuminate the presence of defects is to study singularities of the phase equations associated associated to system (10). We will set these questions aside as subjects for future work.

In R_2 , we observed both spatio-temporal chaos similar to that exhibited by the KS equation, and coarsening. The particular selected behavior seems to depend largely on the relative strengths of the nonlinearities in system (10). When the nonlinear dynamics were dominated by the $\lambda|\nabla u|^2$ term in the first equation of motion and the cubic nonlinearity $\eta\phi^3$ in the second equation of motion, spatio-temporal chaos resulted. Such a solution is shown in figure 6. On the other hand, when we made the $\nu\phi^2$ term in the second equation of motion the dominant quadratic nonlinearity, we observed spatial coarsening, as illustrated in figure 6. Thus, our model replicates the results of Bradley and Shipman in R_2 .

In R_3 , we observed traveling wave solutions, which were caused by an active Hopf mode, as shown in figures 15 and 16. Transient square patterns were also present during the formation of the traveling waves. These simulations suggest the interesting possibility that even during normal incidence ion bombardment, ripple patterns that form during experiments are not stationary at long times, but rather continue to travel until the termination of an experiment. The absence of first order spatial derivative terms in (10), such as those present in the transport equation, leads us to believe that a phase difference in u and ϕ which is between 0 and π is responsible for producing this effect. The phase difference may be observed in figure 17. Further investigation of these traveling wave solutions will require the analysis of phase equations for system (10).

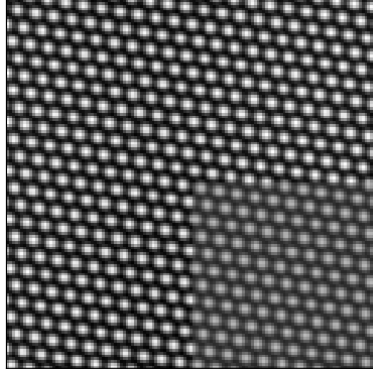


Figure 10: Hexagonal pattern from C_{PS} with parameter values $a = .1$, $b = b_T - 0.05 \approx .8611$, $c = 2.6$, $d = 1$, $\lambda = .1$, $\nu = 1$, $\eta = 0$, $\zeta = 10$, $t = 2000$, $L = 60$. The lower right inset shows ϕ , while the rest of the image shows u . Light shading denotes positive values, and dark shading shows negative values.

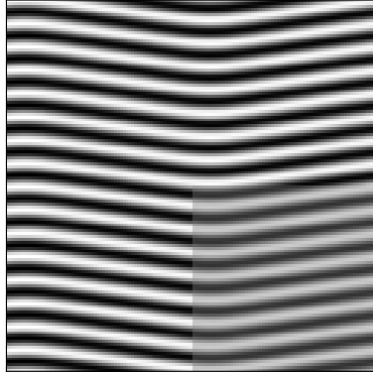


Figure 11: Stripe pattern from C_{PS} with parameter values $a = .1$, $b = b_T - .05 \approx .7792$, $c = 2.25$, $d = .8$, $\lambda = .1$, $\nu = .1$, $\eta = 0$, $\zeta = 10$, $t = 2000$, $L = 40$.

7 Discussion

A number of experiments have shown the formation of hexagonal nanodot lattices in binary materials bombarded at normal incidence [2,3,9,10,29]. As of yet it is unclear whether the more or less preferentially sputtered species accumulates at the maxima of the nanodots. In terms of our notation, the fields u and ϕ are in phase when the less preferentially sputtered species accumulates at peaks, and have a phase difference of π radians when the preferentially sputtered species appears at peaks. Alternatively, we have measured correlation between u and ϕ to gain a sense for whether maxima of u coincide with maxima or minima of ϕ . The formation of defects in experimentally observed nanodot lattices is also common. Typically, these come in the form of “heptapenta defects”, where the regular hexagonal lattice is interrupted by a pair of nearby nanodots, one with five nearest neighbors, and the other with seven. Also common are “grain boundaries”, across which the selected wavevectors which determine the pattern change discontinuously.

Our numerical integrations of system (10) indicate that the nature of the linear instability driving the formation of patterned surface topographies also plays a role in determining the relative phases of surface height and composition. Surface topographies which develop from instabilities driven primarily by the Bradley-Harper effect correspond to solutions of (10) in which the fields u and ϕ are anticorrelated. This reproduces a result already presented by Bradley and Shipman [23]. On the other hand, topographies resulting from a phase separation driven instability correspond to solutions of system (10) in which the fields u and ϕ are entirely in phase. The sign of ϖ in C_{BS} and C_{PS} in our weakly nonlinear analysis of system (10) corroborates this

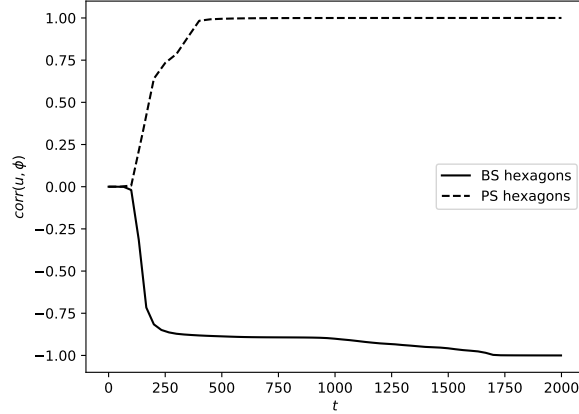


Figure 12: Spatial correlations of u and ϕ as functions of time during formation of hexagonal patterns in C_{BS} and C_{PS}

finding. These theoretical results imply that an experiment designed to measure which species is predominantly located at the peaks of nanodots could provide strong evidence towards which physical mechanism contributes to pattern formation.

Also notable in our numerical results is the presence of hexagonal defects in the Bradley Harper regime, and their apparent absence in the phase separation regime. The high degree of hexagonal order exhibited by phase separation driven topographies deviates from experimental results, which tend to display lower degrees of hexagonal order. Admittedly, we make this point with two caveats. First, our notion of “hexagonal order” is purely qualitative. Second, we have not rigorously proved the non-existence of solutions with defects in the phase separation regime, and are merely relying on simulation data to make this assertion. It is our hope that these concerns may be addressed using tools such as persistent homology from the mathematical discipline of algebraic topology and by studying singularities of a system of phase equations for system (10).

The relative phases of the fields u and ϕ also appears to play a crucial role in the formation of traveling wave solutions to system (10). After an initial transient phase in which squares seem to form, the system converges to a state in which u and ϕ are slightly out of phase. We can reasonably expect this state to lead to traveling waves because a higher concentration of the less-preferentially sputtered species seems to be present just ahead of the wavefront. This finding suggests that patterns that form during ion bombardment experiments may not be stationary with time, even when bombardment occurs at normal incidence.

8 Summary

In this paper we extended the Bradley-Shipman model for normal incidence ion bombardment of binary solids to account for competition between the BH effect and ion-induced phase separation during pattern formation. Motivated by the work of Norris, we began by deriving linear equations of motion describing the evolution of coupled height and concentration fields. We then studied the linear stability of this system, and discovered that Turing instabilities arise in distinct regions of parameter space corresponding to the Bradley-Harper effect and phase separation. We also characterized regions in which Hopf instabilities and long-wavelength Turing instabilities occur. We observed that multiple simultaneous linear instabilities can occur near boundaries of regions in our phase diagram. In order to study pattern formation beyond the linear regime, we added nonlinearities to our model. We investigated the effects of adding these nonlinearities by two means: a weakly nonlinear analysis, and numerical integrations of our equations of motion. Both techniques indicate that the phase difference between surface height and composition can provide evidence towards which physical mechanism is actively contributing to pattern formation for a given binary compound, suggesting a direction for future ion-bombardment experiments. We additionally observed what appeared to be a high degree of hexagonal order in surfaces evolving under the effects of phase separation, and a somewhat lesser degree of hexagonal order for surfaces evolving under a stronger Bradley-Harper effect. However, conclusive evidence that phase separation leads to high degrees of hexagonal order will require further mathematical analysis.

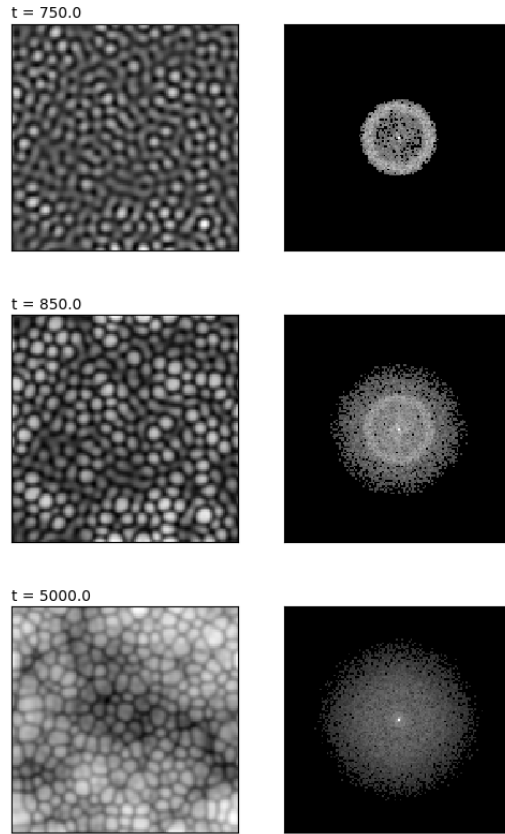


Figure 13: Spatio-temporal chaos in R_2 at parameters $a = 1$, $b = .75$, $c = 1$, $d = 1.25$, $\lambda = 1$, $\nu = 0$, $\eta = 10$, $\zeta = 0$.

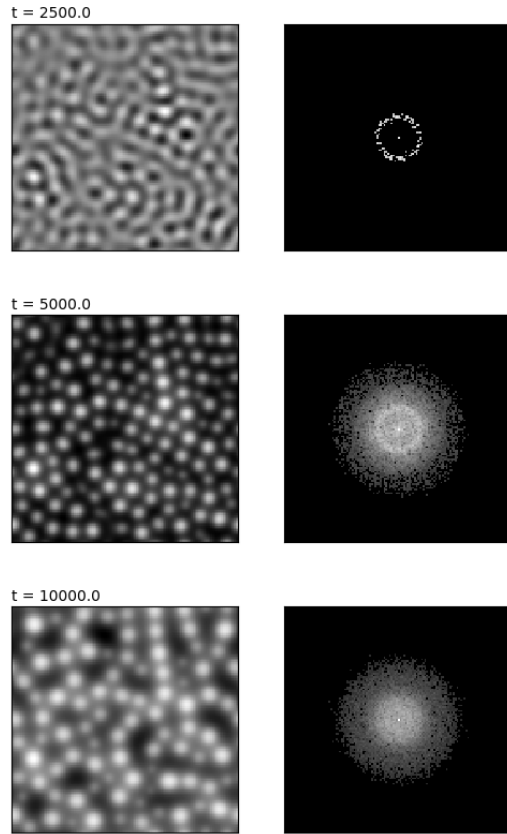


Figure 14: Coarsening in R_2 at parameters $a = 1$, $b = .875$, $c = 1$, $d = 1.25$, $\lambda = 0$, $\nu = 2$, $\eta = 10$, $\zeta = 0$.

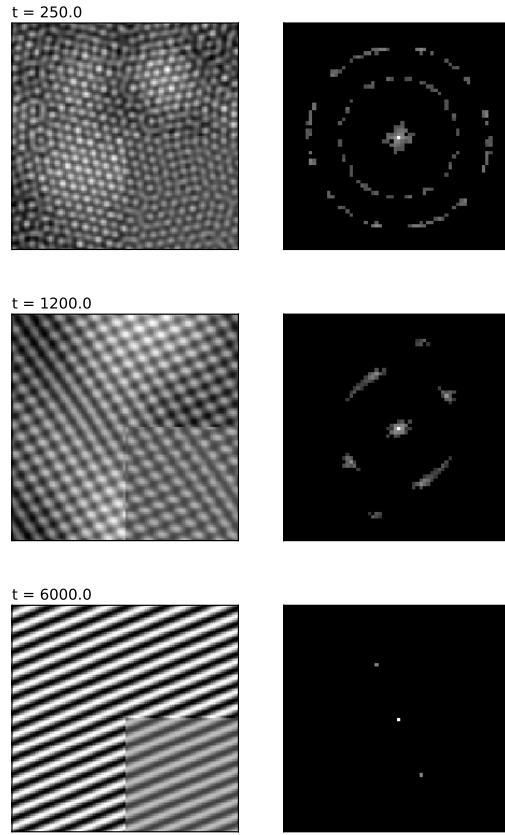


Figure 15: Time series data from a simulation in R_3 . The left column shows u , with ϕ inset. The right column shows the power spectral density function for u .

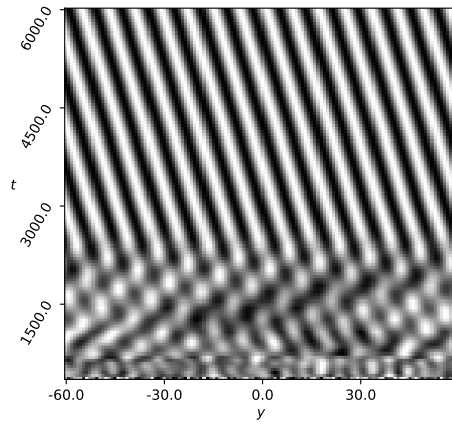


Figure 16: Spacetime plot of u from the traveling wave solution shown in figure 15.

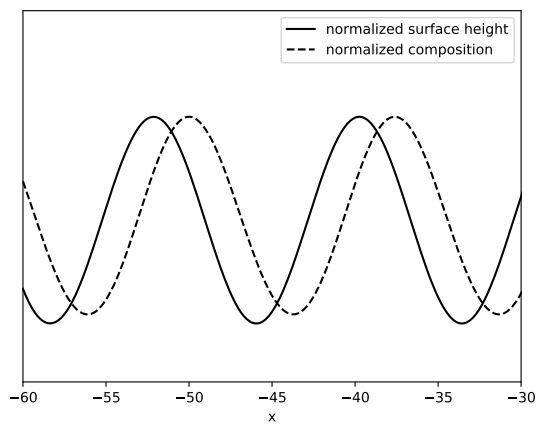


Figure 17: Normalized cross sections of u and ϕ at $t = 6000$ from the solution shown in figure 15.

Appendix A: Python 2 Implementation of Numerical Method

```
from __future__ import division
import numpy as np
from numpy.fft import rfft2,irfft2
import math
from numpy.random import rand, randn, seed
from scipy.fftpack import fftshift,fftfreq
from scipy.integrate import simps,trapz,quad
import shutil
import time
import sys
import pdb

#solves the system of evolution equations
#u_t = v - a*grad^2*u - grad^2grad^2*u + lamda*(grad u)^2
#v_t = -v + b*grad^2*u - c*grad^2*v - d*grad^2grad^2*v + nu*v^2 + eta*v^3 + zeta*grad^2*v^3

def solve_ps(N,Nfinal,h,ckeep,L,a,b,c,d,lamda,nu,eta,zeta,filename = None):

    print 'initializing ps_etdrk4'
    print 'N = %s' % N
    print 'Nfinal = %s' %Nfinal
    print 'h = %s' %h
    print 'ckeeep = %s' %ckeeep
    print 'L = %s' %L
    print 'a = %s' %a
    print 'b = %s' %b
    print 'c = %s' %c
    print 'd = %s' %d
    print 'lamda = %s' %lamda
    print 'nu = %s' %nu
    print 'eta = %s' %eta
    print 'zeta = %s' %zeta

    u,v = np.array((1e-3)*rand(N,N)), np.array((1e-3)*rand(N,N))#initial conditions
    uhat = rfft2(u)
    vhat = rfft2(v)
    ukeep = np.empty((1 + int(Nfinal/ckeeep),N,N))
    ukeep[0,:,:] = u
    vkeep = np.empty((1 + int(Nfinal/ckeeep),N,N))
    vkeep[0,:,:] = v
    tkeep = h*np.arange(0,Nfinal+1,ckeeep)
    ky = np.pi/L*fftshift(np.arange(-N/2,N/2))
    kx = np.pi/L*np.arange(N/2+1)
    kxx,kyy = np.meshgrid(kx,ky)
    ksq = kxx**2 + kyy**2

    #Diagonal entries of the linear operators Lt and Lt/2
    Lu = h*(a*ksq - ksq**2)
    Lu2 = 0.5*Lu
    Lv = h*(-1 + c*ksq-d*ksq**2)
    Lv2 = 0.5*Lv

    M = 32#number of points to use in complex contour integral
    t = np.linspace(0,np.pi,M)
    rts = np.exp(1j*t)
    #computes f(L) using contour integral over circle of radius 1 centered at L
    def evaluate(f,L):
        integrand = f(L.reshape((L.shape[0],L.shape[1],1)) + rts)
        return np.real(np.trapz(integrand,dx=np.pi/(M-1)))/np.pi
```

```

coeff_start = time.time()

#functions kappa, alpha, beta, and gamma are defined at bottom,
# and are taken from Trefethen, Kassam, 2005
kappa_u = evaluate(kappa,Lu2)
kappa_v = evaluate(kappa,Lv2)
alpha_u = evaluate(alpha,Lu)
alpha_v = evaluate(alpha,Lv)
beta_u = evaluate(beta,Lu)
beta_v = evaluate(beta,Lv)
gamma_u = evaluate(gamma,Lu)
gamma_v = evaluate(gamma,Lv)

coeff_end = time.time()
coeff_time = coeff_end - coeff_start
print 'Coefficients computed in %s seconds' % coeff_time

def periodic_gradient(u,dx):
    u_ext = np.zeros((u.shape[0]+4,u.shape[1]+4))
    u_ext[2:N+2,2:N+2] = u
    u_ext[2:N+2,N+2:] = u[:,0:2]
    u_ext[2:N+2,0:2] = u[:,N-2:]
    u_ext[N+2:,2:N+2] = u[0:2,:]
    u_ext[0:2,2:N+2] = u[N-2:,:]
    u_ext[N+2:,N+2:] = u[0:2,0:2]
    u_ext[0:2,N+2:] = u[N-2:,0:2]
    u_ext[N+2:,0:2] = u[0:2,N-2:]
    u_ext[0:2,0:2] = u[N-2:,N-2:]
    uy_ext,ux_ext = np.gradient(u_ext,dx)
    uy = uy_ext[2:N+2,2:N+2]
    ux = ux_ext[2:N+2,2:N+2]
    return uy,ux

def rhs(u,v): #Nonlinear parts of the original pde
    uy,ux = periodic_gradient(u,2*L/N)
    v3 = v**3
    v3y,v3x = periodic_gradient(v3,2*L/N)
    v3yy,v3yx = periodic_gradient(v3y,2*L/N)
    v3xy,v3xx = periodic_gradient(v3x,2*L/N)
    return lamda*(ux**2 + uy**2), nu*v**2 + eta*v3 + zeta*(v3xx + v3yy)

#nonlinear operator on Fourier space
def nonlinear(uhat,vhat):
    u = irfft2(uhat)
    v = irfft2(vhat)
    u,v = rhs(u,v)
    return rfft2(u) + vhat,rfft2(v)-b*ksq*uhat

#diagonal entries of matrix exponential exp(Lt)
eu2 = np.exp(Lu2)
eu = np.exp(Lu)
ev2 = np.exp(Lv2)
ev = np.exp(Lv)
#etdrk4 time stepping loop

loop_start = time.time()
for n in range(1,Nfinal+1):

    Nu,Nv = nonlinear(uhat,vhat)
    #the multiplicative factor of 0.5*h is to account for the discrepancy in

```

```

#the Cox/Matthews ETDK4 formula and our coefficients after we have evaluated kappa
au = eu2*uhat + 0.5*h*kappa_u*Nu
av = ev2*vhat + 0.5*h*kappa_v*Nv

Nau,Nav = nonlinear(au,av)
bu = eu2*uhat + 0.5*h*kappa_u*Nau
bv = ev2*vhat + 0.5*h*kappa_v*Nav

Nbu,Nbv = nonlinear(bu,bv)
cu = eu2*au + .5*h*kappa_u*(2*Nbu-Nu)
cv = ev2*av + .5*h*kappa_v*(2*Nbv-Nv)

Ncu,Ncv = nonlinear(cu,cv)

uhat = rfft2(irfft2(eu*uhat + h*alpha_u*Nu + 2*h*beta_u*(Nau + Nbu) + h*gamma_u*Ncu))
vhat = rfft2(irfft2(ev*vhat + h*alpha_v*Nv + 2*h*beta_v*(Nav + Nbv) + h*gamma_v*Ncv))

try:
    if np.isnan(uhat).any() or np.isnan(vhat).any():
        raise ValueError('Solution Contains NaN')
except ValueError as error:
    print(error.args)
    break

if int(n%ckeepp) == 0:

    ukeep[int(n/ckeepp),:,:] = irfft2(uhat)
    vkeep[int(n/ckeepp),:,:] = irfft2(vhat)

loop_end = time.time()
loop_time = loop_end-loop_start
print 'ETDRK4 loop completed in %s seconds' % loop_time

if filename == None:
    filename = ('phase_sep_etdrk4_' + time.strftime('%m_%d_%Y_%H_%M') + '_a_'
        + str(a) + '_b_' + str(b) + '_c_' + str(c) + '_d_'
        + str(d) + '_L_' + str(L) + '_N_' + str(N) + '_h_' + str(h))
    filename = filename.replace('.', '_').replace('-', 'm')
    filename = filename + '.npz'
    filename = 'solutions/' + filename

np.savez(filename,N = N,Nfinal= Nfinal,h = h,ckeepp = ckeepp,L = L,
    a = a,b = b,c = c, d = d,lamda = lamda,nu = nu,eta = eta,
    zeta = zeta, u = ukeep, v = vkeep, t = tkeep)

#functions used to compute coefficients before the main loop

def kappa(z):
    return (np.exp(z) - 1)/z

def alpha(z):
    return (-4-z+np.exp(z)*(4-3*z + z**2))/(z**3)

def beta(z):
    return (2 + z + np.exp(z)*(-2 + z))/(z**3)

def gamma(z):
    return (-4 - 3*z - z**2 + np.exp(z)*(4-z))/(z**3)

if __name__ == '__main__':

```



```

a = float(sys.argv[1])
b = float(sys.argv[2])
c = float(sys.argv[3])
d = float(sys.argv[4])
lamda = float(sys.argv[5])
nu = float(sys.argv[6])
eta = float(sys.argv[7])
zeta = float(sys.argv[8])
N = int(sys.argv[9])
h = float(sys.argv[10])
t_final = float(sys.argv[11])
number_stored_solutions = int(sys.argv[12])
L = float(sys.argv[13])

Nfinal = int(t_final/h)
ckeep = int(Nfinal/number_stored_solutions)
t_start = time.time()
#pdb.set_trace()
solve_ps(N,Nfinal,h,ckeeep,L,a,b,c,d,lamda,nu,eta,zeta)
t_end = time.time()
runtime = t_end - t_start
print 'runtime: %s seconds' % runtime

```

Appendix B: Computation of L_0^\dagger

We now verify that L_0^\dagger is as given in section 4.

Lemma 8.1 *Let \mathcal{P} , V , H , and L_0 be as defined in section 4. The adjoint operator of L_0 is given by*

$$L_0^\dagger = \begin{pmatrix} \frac{\partial}{\partial t_0} + a\nabla^2 + \nabla^2\nabla^2 & -b_T\nabla^2 \\ -1 & \frac{\partial}{\partial t_0} + 1 + c\nabla^2 + d\nabla^2\nabla^2 \end{pmatrix}.$$

Proof 8.2 *The adjoint satisfies $\langle \mathbf{v}, L_0 \mathbf{w} \rangle = \langle L_0^\dagger \mathbf{v}, \mathbf{w} \rangle$ for all $\mathbf{v}, \mathbf{w} \in H$. Let $\mathbf{v} = (v_1, v_2)^T$ and $\mathbf{w} = (w_1, w_2)^T$ be elements of H . Let $dA = dx dy$ and $d\sigma$ be an appropriate differential form on the boundary of \mathcal{P} , and let \mathbf{n} be an outward pointing normal vector field on $\partial\mathcal{P}$. Observe that for any $f, g \in V$, we have by repeated application of Green's first identity*

$$\begin{aligned}
\int_{\mathcal{P}} f \nabla^2 g \, dA &= \int_{\partial\mathcal{P}} f(\nabla g \cdot \mathbf{n}) \, d\sigma - \int_{\mathcal{P}} \nabla f \cdot \nabla g \, dA \\
&= - \int_{\mathcal{P}} \nabla f \cdot \nabla g \, dA \\
&= - \int_{\partial\mathcal{P}} (\nabla f \cdot \mathbf{n}) g \, d\sigma + \int_{\mathcal{P}} (\nabla^2 f) g \, dA \\
&= \int_{\mathcal{P}} (\nabla^2 f) g \, dA.
\end{aligned}$$

Similarly,

$$\int_{\mathcal{P}} f \nabla^2 \nabla^2 g \, dA = \int_{\mathcal{P}} (\nabla^2 \nabla^2 f) g \, dA.$$

In terms of the inner product on V , this says that $\langle f, \nabla^2 g \rangle_V = \langle \nabla^2 f, g \rangle_V$ and $\langle f, \nabla^2 \nabla^2 g \rangle_V = \langle \nabla^2 \nabla^2 f, g \rangle_V$.

Now, let $\mathbf{f}_1 = (1, 0)^T$ and $\mathbf{f}_2 = (0, 1)^T$. We compute $\langle L_0^\dagger(v_i \mathbf{f}_i), w_j \mathbf{f}_j \rangle_H$ for $i, j = 1, 2$.

$$\begin{aligned}
\langle L_0^\dagger(v_1 \mathbf{f}_1), w_1 \mathbf{f}_1 \rangle_H &= \langle v_1 \mathbf{f}_2, L_0(w_1 \mathbf{f}_1) \rangle_H \\
&= \langle v_1, (a \nabla^2 + \nabla^2 \nabla^2) w_1 \rangle_V \\
&= \langle (a \nabla^2 + \nabla^2 \nabla^2) v_1, w_1 \rangle_V \\
&= \langle (a \nabla^2 + \nabla^2 \nabla^2) v_1 \mathbf{f}_1, \mathbf{w} \rangle_H, \\
\langle L_0^\dagger(v_1 \mathbf{f}_1), w_2 \mathbf{f}_2 \rangle_H &= \langle v_1 \mathbf{f}_1, w_2 \mathbf{f}_2 \rangle_H \\
&= \langle v_1, -w_2 \rangle_V \\
&= \langle -v_1, w_2 \rangle_V \\
&= \langle -v_1 \mathbf{f}_1, \mathbf{w} \rangle_H \\
\langle L_0^\dagger(v_2 \mathbf{f}_2), w_1 \mathbf{f}_1 \rangle_H &= \langle v_2 \mathbf{f}_2, L_0(w_1 \mathbf{f}_1) \rangle_H \\
&= \langle v_2, -b_T \nabla^2 w_1 \rangle_V \\
&= \langle -b_T \nabla^2 v_2, w_1 \rangle_V \\
&= \langle -b_T \nabla^2 (v_2 \mathbf{f}_1), \mathbf{w} \rangle_H,
\end{aligned}$$

and

$$\begin{aligned}
\langle L_0^\dagger(v_2 \mathbf{f}_2), w_2 \mathbf{f}_2 \rangle_H &= \langle v_2 \mathbf{f}_2, L_0(w_2 \mathbf{f}_2) \rangle_H \\
&= \langle v_2, (1 + c \nabla^2 + d \nabla^2 \nabla^2) w_2 \rangle_V \\
&= \langle (1 + c \nabla^2 + d \nabla^2 \nabla^2) v_2, w_2 \rangle_V \\
&= \langle (1 + c \nabla^2 + d \nabla^2 \nabla^2) v_2 \mathbf{f}_2, \mathbf{w} \rangle_H
\end{aligned}$$

We now have

$$\begin{aligned}
\langle L_0^\dagger(v_1 \mathbf{f}_1), \mathbf{w} \rangle_H &= \langle L_0^\dagger(v_1 \mathbf{f}_1), w_1 \mathbf{f}_1 \rangle_H + \langle L_0^\dagger(v_1 \mathbf{f}_1), w_2 \mathbf{f}_2 \rangle_H \\
&= \langle (a \nabla^2 + \nabla^2 \nabla^2) v_1 \mathbf{f}_1, \mathbf{w} \rangle_H + \langle -v_1 \mathbf{f}_2, \mathbf{w} \rangle_H \\
&= \langle (a \nabla^2 + \nabla^2 \nabla^2) v_1 \mathbf{f}_1 - v_1 \mathbf{f}_2, \mathbf{w} \rangle_H
\end{aligned}$$

and

$$\begin{aligned}
\langle L_0^\dagger(v_2 \mathbf{f}_2), \mathbf{w} \rangle_H &= \langle L_0^\dagger(v_2 \mathbf{f}_2), w_1 \mathbf{f}_1 \rangle_H + \langle L_0^\dagger(v_2 \mathbf{f}_2), w_2 \mathbf{f}_2 \rangle_H \\
&= \langle -b_T \nabla^2 (v_2 \mathbf{f}_1), \mathbf{w} \rangle_H \\
&+ \langle (1 + c \nabla^2 + d \nabla^2 \nabla^2) v_2 \mathbf{f}_2, \mathbf{w} \rangle_H \\
&= \langle -b_T \nabla^2 (v_2 \mathbf{f}_1) + (1 + c \nabla^2 + d \nabla^2 \nabla^2) (v_2 \mathbf{f}_2), \mathbf{w} \rangle_H.
\end{aligned}$$

Thus $L_0^\dagger(v_1 \mathbf{f}_1) = (a \nabla^2 + \nabla^2 \nabla^2)(v_1 \mathbf{f}_1) - v_1 \mathbf{f}_2$, and $L_0^\dagger(v_2 \mathbf{f}_2) = -b_T \nabla^2 (v_2 \mathbf{f}_1) + (1 + c \nabla^2 + d \nabla^2 \nabla^2)(v_2 \mathbf{f}_2)$, from which it follows that

$$L_0^\dagger = \begin{pmatrix} a \nabla^2 + \nabla^2 \nabla^2 & -b_T \nabla^2 \\ -1 & 1 + c \nabla^2 + d \nabla^2 \nabla^2 \end{pmatrix}.$$

References

- [1] Bruce A Banks, Albert J Weigand, Charles A Babbush, and CL Vankampen. Potential biomedical applications of ion beam technology. 1976.
- [2] L Bischoff, K-H Heinig, B Schmidt, S Facsko, and W Pilz. Self-organization of ge nanopattern under erosion with heavy bi monomer and cluster ions. *Nuclear Instruments and Methods in Physics Research Section B: Beam Interactions with Materials and Atoms*, 272:198–201, 2012.
- [3] L Bischoff, W Pilz, and B Schmidt. Amorphous solid foam structures on germanium by heavy ion irradiation. *Applied Physics A: Materials Science & Processing*, 104(4):1153–1158, 2011.
- [4] R Mark Bradley and James ME Harper. Theory of ripple topography induced by ion bombardment. *Journal of Vacuum Science & Technology A: Vacuum, Surfaces, and Films*, 6(4):2390–2395, 1988.
- [5] Steven M Cox and Paul C Matthews. Exponential time differencing for stiff systems. *Journal of Computational Physics*, 176(2):430–455, 2002.
- [6] R Craster, R Sassi, et al. Spectral algorithms for reaction-diffusion equations. 2006.

- [7] Michael Cross and Henry Greenside. *Pattern formation and dynamics in nonequilibrium systems*. Cambridge University Press, 2009.
- [8] Rashmi Desai and Raymond Kapral. *Dynamics of self-organized and self-assembled structures*. Cambridge University Press, 2009.
- [9] S. Facsko, T. Dekorsy, C. Koerdts, C. Trappe, H. Kurz, A. Vogt, and H. L. Hartnagel. Formation of ordered nanoscale semiconductor dots by ion sputtering. *Science*, 285(5433):1551–1553, 1999.
- [10] Monika Fritzsche, Arndt Muecklich, and Stefan Facsko. Nanohole pattern formation on germanium induced by focused ion beam and broad beam Ga^+ irradiation. *Applied Physics Letters*, 100(22):223108, 2012.
- [11] Matt P Harrison and R Mark Bradley. Crater function approach to ion-induced nanoscale pattern formation: Craters for flat surfaces are insufficient. *Physical Review B*, 89(24):245401, 2014.
- [12] Rebecca B Hoyle. *Pattern formation: an introduction to methods*. Cambridge University Press, 2006.
- [13] Aly-Khan Kassam and Lloyd N Trefethen. Fourth-order time-stepping for stiff pdes. *SIAM Journal on Scientific Computing*, 26(4):1214–1233, 2005.
- [14] A. Keller, O. Z. Andersen, M. Foss, S. Facsko, D. C. Kraft, and F. Besenbacher. Response of human mesenchymal stem cells to nanopatterned surfaces. abstract and presentation at the workshop *Nanoscale Pattern Formation at Surfaces*, El Escorial, Spain (2011)., 2011.
- [15] Francois Leonard and Rashmi C Desai. Chemical ordering during surface growth. *Physical Review B*, 55(15):9990, 1997.
- [16] William W Mullins. Theory of thermal grooving. *Journal of Applied Physics*, 28(3):333–339, 1957.
- [17] M Navez, C Sella, and D Chaperot. Investigation of the attack on glass by ion bombardment. *C. R. Acad. Sci. Paris*, 254:240–244, 1962.
- [18] Scott A Norris. Ion-assisted phase separation in compound films: An alternate route to ordered nanostructures. *Journal of Applied Physics*, 114(20):204303, 2013.
- [19] Scott A Norris, Michael P Brenner, and Michael J Aziz. From crater functions to partial differential equations: a new approach to ion bombardment induced nonequilibrium pattern formation. *Journal of Physics: Condensed Matter*, 21(22):224017, 2009.
- [20] Scott A Norris, Juha Samela, Matias Vestberg, Kai Nordlund, and Michael J Aziz. Crater functions for compound materials: A route to parameter estimation in coupled-pde models of ion bombardment. *Nuclear Instruments and Methods in Physics Research Section B: Beam Interactions with Materials and Atoms*, 318:245–252, 2014.
- [21] Thomas WH Oates, Adrian Keller, Stefan Facsko, and Arndt Muecklich. Aligned silver nanoparticles on rippled silicon templates exhibiting anisotropic plasmon absorption. *Plasmonics*, 2(2):47–50, 2007.
- [22] VB Shenoy, WL Chan, and E Chason. Compositionally modulated ripples induced by sputtering of alloy surfaces. *Physical review letters*, 98(25):256101, 2007.
- [23] Patrick D Shipman and R Mark Bradley. Theory of nanoscale pattern formation induced by normal-incidence ion bombardment of binary compounds. *Physical Review B*, 84(8):085420, 2011.
- [24] Peter Sigmund. A mechanism of surface micro-roughening by ion bombardment. *Journal of Materials Science*, 8(11):1545–1553, 1973.
- [25] C Teichert, JJ De Miguel, and T Bobek. Ion beam sputtered nanostructured semiconductor surfaces as templates for nanomagnet arrays. *Journal of Physics: Condensed Matter*, 21(22):224025, 2009.
- [26] Elizabeth J Tocce, Valery K Smirnov, Dmitry S Kibalov, Sara J Liliensiek, Christopher J Murphy, and Paul F Nealey. The ability of corneal epithelial cells to recognize high aspect ratio nanostructures. *Biomaterials*, 31(14):4064–4072, 2010.
- [27] Lloyd N Trefethen. *Spectral methods in MATLAB*. SIAM, 2000.
- [28] Kaier Wang, Moira L Steyn-Ross, D Alistair Steyn-Ross, and Marcus T Wilson. Derivation of the amplitude equation for reaction–diffusion systems via computer-aided multiple-scale expansion. *International Journal of Bifurcation and Chaos*, 24(07):1450101, 2014.

- [29] Qiangmin Wei, Xiuli Zhou, Bhuwan Joshi, Yanbin Chen, Kun-Dar Li, Qihuo Wei, Kai Sun, and Lumin Wang. Self-assembly of ordered semiconductor nanoholes by ion beam sputtering. *Advanced Materials*, 21(28):2865–2869, 2009.